Research Article

Optical properties of heat-treated hierarchical structure of Eu^{3+} modified C-$CaIn_2O_4$ of small core–shell crystallites

Barkha Tiwari[1] · **Shanker Ram**[1]

Received: 18 November 2019 / Accepted: 10 March 2020 / Published online: 13 March 2020

Abstract
A natural aloe-vera gel is promptly bridging the Eu^{3+}, Ca^{2+} and In^{3+} species in a bio-complex of a polymer network, so as it yields a sample Eu^{3+}:$CaIn_2O_4$ of small crystallites bonding over a grafted C-sp^2 surface layer when it is burnt in a self-propagating combustion in air. The Eu^{3+} doped C-$CaIn_2O_4$ sample appears in a core–shell structure in part of the carbon forming a conjoint surface layer (shell) thereon of the individual crystallites in a hybrid nanostructure. The results are analyzed in terms of XRD patterns, phonon bands (in IR and Raman spectra), XPS bands, and hierarchical microstructure in the samples prepared with different Eu^{3+} dosages in finely tuning the microstructure and optical properties as useful for an efficient phosphor, optical display system, visible lasers, energy-converters, photocatalysts, optical imaging, medical tools, and several others. A partial $Eu^{3+} \rightarrow In^{3+}$ doping in a crystal lattice $CaIn_2O_4$ clearly reflects in a marked expansion of the lattice, as much as 2.2% found in the Eu^{3+} content progressively raised to 2.0 mol% in a tailored hybrid composite structure. An inbuilt C-sp^2 shell structure of the crystallites is characterized in terms of its characteristic phonon bands in a conjoint polymer network, which are accounted well in modified XPS bands in the surface species.

✉ Barkha Tiwari, barkha@matsc.iitkgp.ernet.in | [1]Materials Science Centre, Indian Institute of Technology, Kharagpur 721302, India.

SN Applied Sciences (2020) 2:646 | https://doi.org/10.1007/s42452-020-2474-0

Graphic abstract

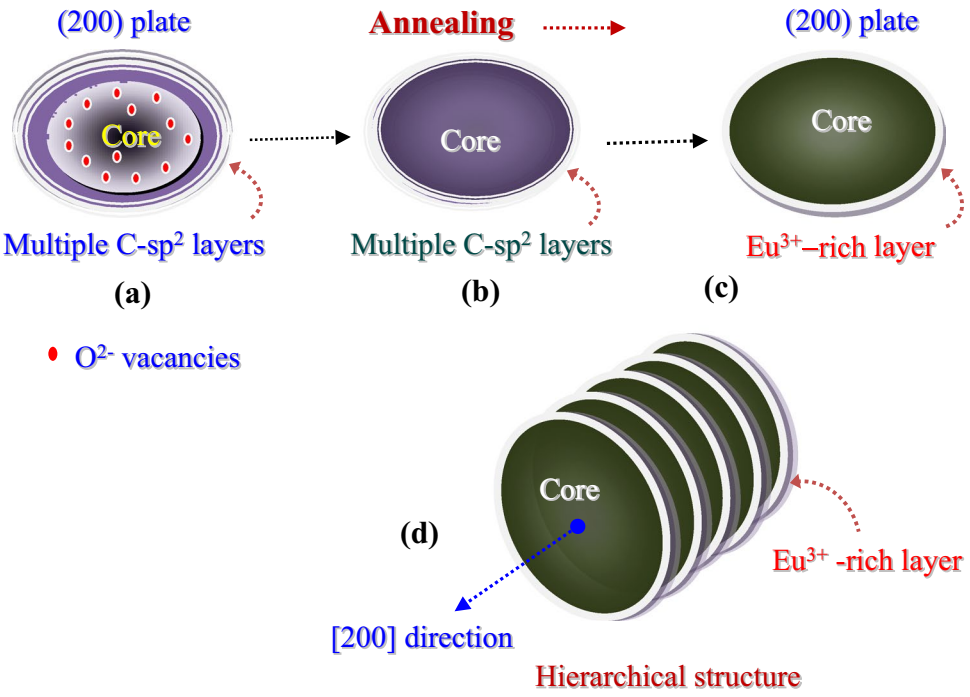

Eu^{3+} Modified C-$CaIn_2O_4$ of Small Core-Shell Crystallites

Keywords Optical properties · Heat-treated · Hierarchical structure · C-$CaIn_2O_4$ · Core–shell crystallites

1 Introduction

The rare-earth ions R^{3+} (for example, R = Nd, Sm, Eu, Tb, Dy, Ho, Er, etc.) are extensively used as an efficient optical dopant to incorporate tunable electronic energy-levels in many engineering oxides like ZnO, ZrO_2, TiO_2, Y_2O_3, Al_2O_3, $ZnAl_2O_4$, $CaAl_2O_4$, $CaIn_2O_4$ etc., so that the later promptly absorb and emit radiation of selective bands in UV, visible, as well as near infrared (NIR) regions [1–10]. Tailored optical and other engineering properties in such R^{3+}-doped oxides have wide spread applications in photonics, lasers, optical witches, optical sensors, and photocatalysis. A unique feature of rare-earths is a specific shell structure of the valence shell of $4f^n$–$5s^2p^6$ electrons in which the valence $4f^n$ electrons (n varies from 1 to 14 over the rare-earth series) are firmly shielded by a completely filled shell of the $5s^2p^6$ electrons, which firmly control them from local microscopic interactions with neighboring ions in a crystal lattice. As a result, they promisingly retain in the characteristically sharp microscopic energy-levels and those do not change much either by changing the mother compound or a foreign host in a case of a doped material of overall an insulator or a semiconductor. Further, a spin–orbit coupling and local crystal fields result in a series of $^{2S+1}L_J$ multiplet bands. Each $^{2S+1}L_J$ electronic state in a multiplet can spilt into its 'J' levels of a maximum of '2J + 1' sub-energy levels accounting in the local crystal field symmetry of the color-center, as described with different examples elsewhere [1–3].

$CaIn_2O_4$ is one of wide-bandgap semiconductor metal oxides with a energy gap of around 3.9 eV is used conventionally as an optical host in doping various transition or rare-earth elements [11]. An increasing market demand for such optical devices like LEDs, CRTs, PDPs and FEDs is giving new route for better light emitting materials [12]. Traditionally, it has already been synthesized using the solid-state reaction route. Certain demerits like, elevated temperatures of annealing and long reaction time for this material has made a trend for new type of materials and synthesis route. To improve the preparation process, some other approaches have been suggested [10]. To prevent these issues researchers shifted towards the new trend of biosynthesis of materials that incorporates plants as a source of reactant. The advantage to this route is being a

simple method that requires aloe vera gel (green gel containing polysaccharides) instead of any chemical, additionally, time and temperature is less compared to traditional routes and lastly this route gives light quenching at higher concentration ~ 1 mol% which is larger than other chemical routes. In this research paper, we have incorporated green gel from aloe vera plant, which yields crystallites of controlled size and shape [13, 14]. Hence, it is helpful in synthesizing of different nanomaterials.

2 Selection of material and its compositions

2.1 Optimizing Eu^{3+} doping in a core–shell nanostructure

Selective dosage of optical Eu^{3+} ions of x = 0.1, 0.5, 1.0, 1.5 and 2.0 mol% have been chosen tentatively in doping a sample C-$CaIn_2O_4$ made of small crystallites in view of finely tuning the light absorption and emission properties in a sample xEu^{3+}:C-$CaIn_2O_4$ of a hybrid composite structure. A larger Eu^{3+} content is not required over here as it leads to adversely quench the light emission in the UV–visible–NIR regions [15–17]. A technical advantage with a core–shell structure is that it tailors multiple surfaces in small crystallites so as it is promptly promoting light absorption and photocatalytic properties useful for various applications of a functionalized hybrid composite nanostructure.

2.2 Synthesis procedure

A hybrid composite xEu^{3+}:C-$CaIn_2O_4$ was prepared of small core–shell crystallites using the raw materials (1) europium acetate, (2) calcium acetate, (3) indium acetate, and (4) aloe-vera gel in an aqueous medium. A stock indium acetate solution was made of a moderate 0.25 M concentration in a 100 mL of distilled water and admixed in a freshly obtained aloe-vera gel in a typical 1:1 ratio in synthesizing a basic C-$CaIn_2O_4$ phase. Then, a 25 mL of an aqueous solution of calcium acetate (1.0 M concentration) was mixed into the above solution by slowly stirring on a magnetic stirrer to disperse it in a homogenous nanocolloid sample. Finally, a europium acetate solution in water was added in a required volume by continuing the stirring. A sample so obtained was then heated at 80–90 °C in air, forming a viscous hydrogel gel in a hydrothermal reaction of the Eu^{3+}, Ca^{2+}, and In^{3+} species in small tissues of the aloe-vera gel of a biogenic complex. It was observed that an initial greenish color of the sample had changed progressively into a dark brownish color in account of a hydrothermal reaction of the cations with bio-polymers present in the aloe-vera gel over 80–90 min of a reaction time. A mixed hydrogel so obtained stands pretty stable in its visible color for a month or so in open air. A final product xEu^{3+}:C-$CaIn_2O_4$ was recovered as on a dried hydrogel (at room temperature) was burnt in a self-propagating combustion with camphor in open air. A recovered powder in this way was pulverized by grinding in a mortar by a pestle for 10–20 min, and then was washed in a hot water in eliminating any free carbon present in the sample. Different batches of the samples thus were prepared in the Eu^{3+} doping varied as 0, 0.1, 0.5, 1.0, 1.5 and 2.0 mol% in a hybrid composite structure. These samples were annealed at 400–600 °C in a muffle furnace for 1–2 h in air in finely refining a core–shell structure.

2.3 Measurements of C-$CaIn_2O_4$ structure and properties

Using an X-ray diffractometer, X'pertPRO PANalytical having an X-ray beam of CuKα of λ = 0.15410 nm wavelength, to scan the XRD patterns over 20°–80° of diffraction angle 2θ to delineate a single-crystalline Eu^{3+}:C-$CaIn_2O_4$ of as-burnt as well as the annealed powders. The data were collected slowly at small 2θ-intervals under 0.01° in resolving the weak intensity peaks. Surface topology, morphology and size in the Eu^{3+}:C-$CaIn_2O_4$ samples were studied with field emission scanning electron microscopy (FESEM) using a ZEISS EVO 60 FESEM at 5–20 kV acceleration voltages. HRTEM images, SAED patterns and lattice images were studied of the samples mounted on a carbon coated copper grid, using an analytical TEM of FEI—TECNAI G2 20S-TWIN operating at 200 kV. The C-sp^2, as breeds a 2D-network (amorphous) on coherent Eu^{3+}:$CaIn_2O_4$ facets, exhibits multiple D and G-bands in Raman spectra over 1200–1800 cm^{-1} as studied by exciting the samples at 514.5 nm by an Ar^+ ion laser. The XPS bands were calibrated with C1*s* at 284.6 eV to scan binding energies of elements. The light absorption and emission properties were measured using UV–visible spectrophotometer of Perkin –Elmer.

3 Results and discussions

3.1 X-ray diffraction of Eu^{3+} doped C-$CaIn_2O_4$ crystallites

XRD pattern change in a sample Eu^{3+}:C-$CaIn_2O_4$ when thermal annealing it at a moderate 400–600 °C temperature for 2 h in air. For example, Fig. 1a compares XRD patterns measured for a typical 1.0 mol% Eu^{3+}:C-$CaIn_2O_4$ sample of small core–shell crystallites (a) before and after thermal annealing at (b) 400 °C and (c) 600 °C for 2 h in air, wherein part of a residual C-sp^2 surface layer

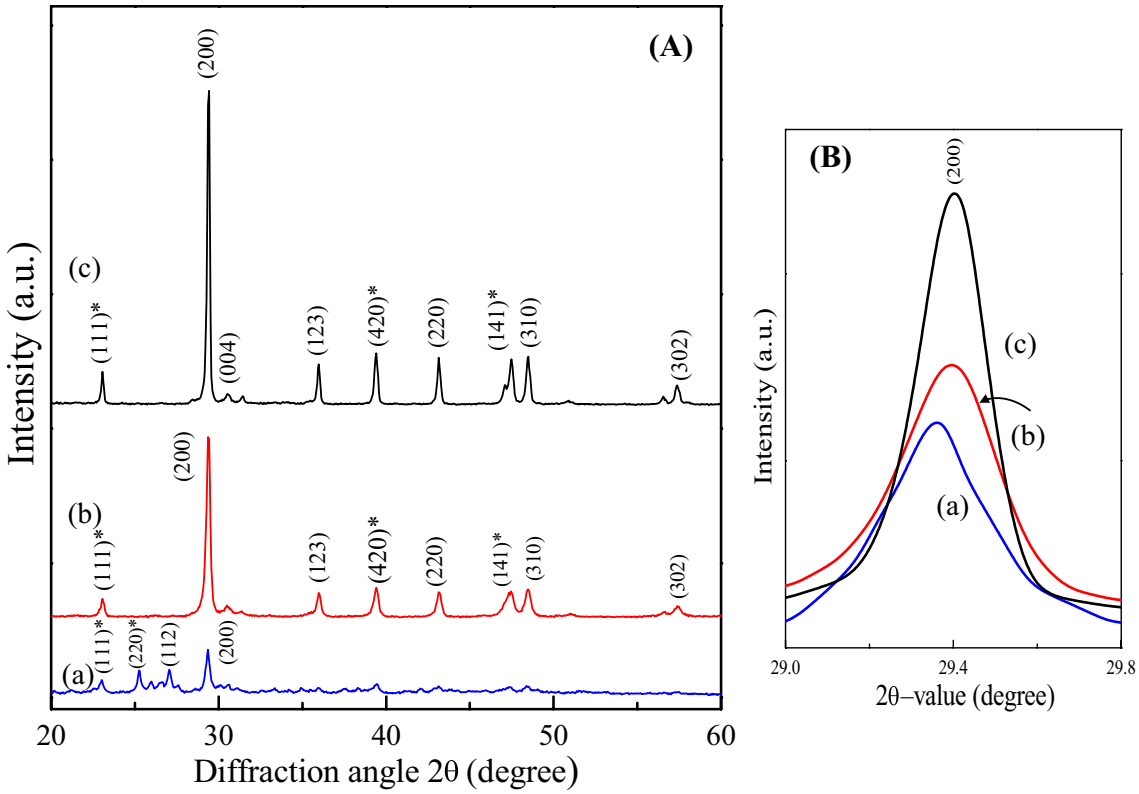

Fig. 1 **A** XRD patterns for (a) as-prepared and annealed 1.0 mol% Eu^{3+}:C-$CaIn_2O_4$ at (b) 400 °C and (c) 600 °C for 2 h in air, with **B** a magnified (200) peak showing how it shifts over larger 2θ-values on thermal annealing

(shell) desorbs off and the bare crystallites start growing in reactive crystallographic facets. The sample is growing preferentially in the (200) planes so as it obtains a larger recurring (200) peak intensity over the master sample at the expense of a residual o-$CaIn_2O_4$ polymorph. Both the peak positions and intensities in the characteristic XRD peaks are tailored in account of a preferential t-$CaIn_2O_4$ growth in the (200) facets in a markedly tailored core–shell structure, which is it is eventually reinforcing a uniaxial high pressure effect propagating on the core with promptly tailored structural parameters as follows. A closer view of the XRD peaks, as can be seen from a magnified (200) peak in Fig. 1b, clearly reveals that the XRD peaks are duly shifting over larger 2θ-values (or smaller d_{hkl} values) in the lattice contacting markedly in growing crystallites in a tailored core–shell structure. In Fig. 1b, the d_{200} value in (200) peak of t-$CaIn_2O_4$ thus has progressively decreased from 0.3053 nm in the as-prepared sample (D = 35 nm) to that at 0.3035 nm in the 400 °C annealed sample (D = 30 nm), while at 0.3033 nm in the 600 °C annealed sample (D = 40 nm), in a markedly tailored surface effect on growth of the small crystallites. A bulk t-$CaIn_2O_4$, as on prepared in a solid state reaction [18], exhibits only a weak (200) peak ($I_p = 3.4$) at a much larger $d_{200} = 0.3107$ nm, possibly involves significant O^{2-} vacancies. In this case, the most intense peak occurs in (211) peak at 0.2674 nm with the second most intense peaks in the diffraction from (202) and (103) planes in markedly different morphology of growth in a bulk polycrystalline t-$CaIn_2O_4$. Other details of the lattice parameters and derived properties from the XRD patterns in a 1.0 mol% Eu^{3+}:C-$CaIn_2O_4$ sample studied before and after the optimal thermal annealing are given in Table 2. When optimally annealed at 400–600 °C in air for 2 h, a sample 1.0 mol% Eu^{3+}:C-$CaIn_2O_4$ has a considerably reduced o-$CaIn_2O_4$ content of 5–10% in its weaker XRD peak intensities. Eventually, a thermal annealing promotes a polymorphic o → t-$CaIn_2O_4$ transformation in a rather easily reordering phase at the expense of thermally mobile O^{2-} vacancies via different oxide polygons in a crystal lattice. The o-$CaIn_2O_4$ shares a rather higher crystal density $\rho_o = 6.144$ g-cm^3 ($V_o = 0.3606$ nm^3) than the t-$CaIn_2O_4$, but a bit lower value than a well-known high-density o-$CaIn_2O_4$ polymorph of $\rho_o = 6.33$ g-cm^3 ($V_o = 0.3500$ nm^3) [18]. A polymorphic o → t change incurs in a bared Eu^{3+}:C-$CaIn_2O_4$ in a critically hot C-sp^2 surface layer destabilizes and releases on heating the sample at 400–600 °C in air. Uniquely, an inbuilt C-sp^2 shell as thinning down in a conjoint network by annealing, the V_t reorders gradually in due shifts (also tailored

intensities) of the XRD peaks in Fig. 1a in annealing an as-burnt Eu^{3+}:C-$CaIn_2O_4$ sample at 400–600 °C in air.

Further, a pretty large intensity of (200) peak in the XRD patterns in Fig. 1a reveals the Eu^{3+}:C-$CaIn_2O_4$ crystallites are grown preferentially in the (200) facets bound in a conjoint (220) surface [19] so as it sharing a second most intense XRD peak at 0.2147 nm in the sample grown in thin plates of the crystallites. Thin sample plates are clearly shown in the HRTEM images as will be discussed later in this chapter. These thin microscopic Eu^{3+}:C-$CaIn_2O_4$ plates are grown in support of a model planar biogenic template binding Eu^{3+}, Ca^{2+}, and In^{3+} species in small bio-polymer chains (from an aloe-vera gel) used in a hydrothermal reaction in this work. Average lattice parameters given in Table 1 fairly produce d_{hkl} values in the observed XRD peaks within a small deviation ±0.0005 nm of an error in the measured values in the different samples. Eventually, an interstitial $Eu^{3+} \rightarrow In^{3+}$ doping causes a Eu^{3+}:$CaIn_2O_4$ lattice to be expanding in its average volume, i.e., as much as $V_t = 0.4302$ nm^3 (density $\rho_t = 5.153$ g-cm^3) found in a 600 °C annealed sample over a bulk $CaIn_2O_4$ value of $V_t = 0.3800$ nm^3 ($\rho_t = 5.833$ g-cm^3) as given in Table 1.

The present microscopic results imply that a thermal annealing causes (1) a C-sp^2 surface layer (shell) thin down gradually in its network structure, (2) a hot C-sp^2 network readily reorder on conjoined Eu^{3+}:$CaIn_2O_4$ facets, (3) a bare $CaIn_2O_4$ to be growing-up slowly, (4) mobile interstitial O^{2-} vacancies reorder in the oxide polygons, and (5) part of interstitial Eu^{3+} species segregate and precipitate onto reactive $CaIn_2O_4$ facets in a modified core–shell structure at reaction temperature. As a fact, a shortened $d_{200} = 0.3053$ nm appears in a uniaxial compression along *a*-axis in the as-prepared sample ($\rho_t = 5.762$ g-cm^3), which is dropped down further to 0.3035 nm in a 400 °C annealed sample ($\rho_t = 5.153$ g-cm^3), or 0.3033 nm in a 600 °C annealed sample ($\rho_t = 5.155$ g-cm^3) in comparison to a bulk 0.3107 nm value ($\rho_t = 5.833$ g-cm^3). In compensating an average V_t value, the *c*-axis is expanding in a way the aspect ratio *c*/*a* increasing in a reduced tetragonality, showing a minimal $c/a = 1.6898$ in the as-prepared sample, which is raised to 1.9255 in the 400 °C annealed sample, or 1.9258 in the 600 °C annealed sample in a finely refined core–shell structure of small crystallites. A far lower $c/a = 1.5838$ persists in a bulk $CaIn_2O_4$ in a 3.7% larger *a*-value. A uniaxial compressed Eu^{3+}:$CaIn_2O_4$ lattice yields a duly large γ = 0.65% in the as-prepared sample, which is grown further to 0.88% in the 400 °C annealed sample, or 0.72% in the 600 °C annealed sample. The present γ-values are estimated from asymmetric broadening (β) in the XRD peaks in the Williamson-Hall plot [20], $\gamma = \beta\cos\theta - \lambda(D\sin\theta)^{-1}$. So obtained D-values in the different samples are included in Table 1.

Here, an open question remains why an average crystal lattice volume is decreased largely in the Eu^{3+}:$CaIn_2O_4$ samples when annealed at 400–600 °C in air. It sounds that the as-prepared sample Eu^{3+}:$CaIn_2O_4$ contains a significant number of O^{2-} vacancies, as marked in a model core–shell in a shape of a plate in Fig. 2a, according to its extended volume. These vacancies were created in a redox reaction with a hot carbon (which captures oxygen from the lattice and escapes as its oxide, $C + O \rightarrow CO\uparrow$) while burning the sample precursor in camphor to remove the byproduct species. Thermally mobile O^{2-} vacancies in the lattice captures Eu^{3+} species from the nearby interstitial sites and ultimately segregate and precipitate onto the reactive surfaces in the individual crystallites. This is shown schematically in Fig. 2b, c. In a due course of an optimal thermal annealing the sample at 400 °C in air, it replaces part of an inbuilt C-sp^2 surface layer of a rigid polymer network thereby in the individual crystallites in the form of a modified Eu^{3+}-rich surface layer in a refined core–shell Eu^{3+}:$CaIn_2O_4$ structure. Here, a migration of both the O^{2-} vacancies and Eu^{3+} ions (of characteristically large ionic sizes) from the lattice core to its surfaces well accounts in a progressively decreased lattice volume in a locally refined microscopic structure in this way as that is what it is observed in XRD in Fig. 1 in the annealed samples. Further, thermodynamically, so small crystallites do expand in the average lattice volume on predominating surfaces in a high Gibbs-free-energy above the equilibrium bulk value [21, 22], but here in this example of a hybrid core–shell structure at the same time owes a competing surface-effect of a rigid core–shell of small crystallites adversely more effectively compressing the lattice in a reasonably lower volume. Such core–shell crystallites cross-link one another via the surface layers in small

Table 1 A microscopic effect of thermal annealing on structural parameters in preferentially grown 1.0 mol% Eu^{3+}:$CaIn_2O_4$ of small core–shell crystallites

1.0 mol% Eu^{3+}:C-$CaIn_2O_4$	Lattice parameters (nm)			D (nm)	V_t (nm^3)	ρ (g-cm^{-3})	γ (%)
	a	*c*	*c*/*a*				
As-prepared	0.6106	1.0318	1.6898	35	0.3847	5.762	0.65
400 °C annealed	0.6068	1.1684	1.9255	30	0.4302	5.153	0.88
600 °C annealed	0.6065	1.1680	1.9258	40	0.4296	5.160	0.72
Bulk $CaIn_2O_4$[a]	0.6214	0.9842	1.5838	–	0.3800	5.833	–

[a]The values are reported from JCPDS file in Ref. [19]

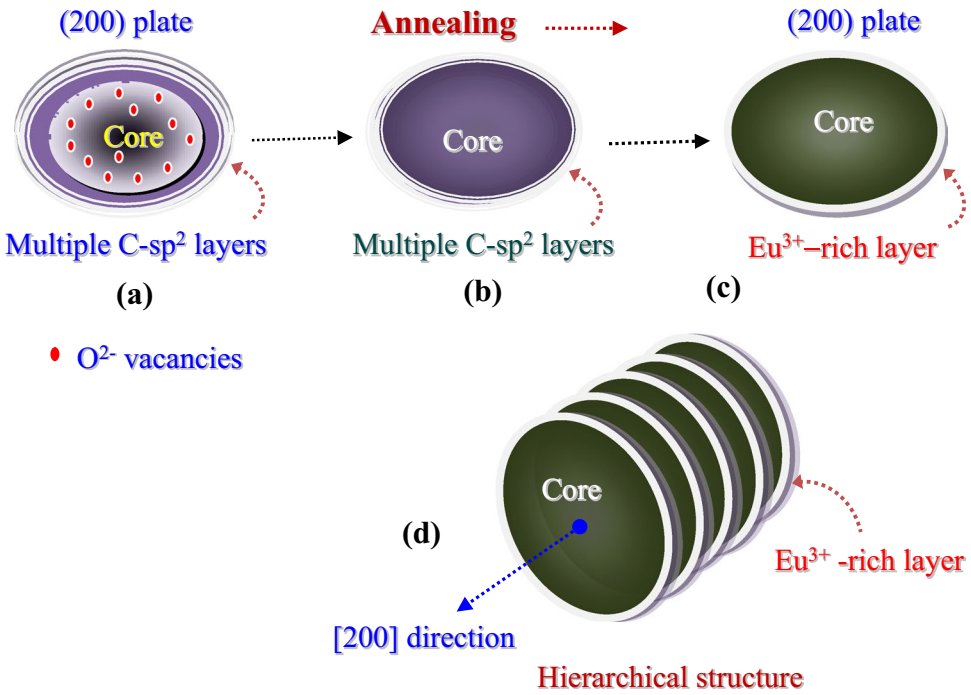

Fig. 2 A model structure of reordering of **a** an inbuilt C-sp^2 surface layer (shell) followed by growth of **b**, **c** a Eu^{3+}-rich layer on preferentially growing Eu^{3+} doped $CaIn_2O_4$ crystallites in (200) plates in **d** a core–shell hierarchical structure

self-assemblies of a "second level hierarchical structure" as shown schematically in a microscopic model in Fig. 2d.

3.2 Phonon bands of Eu^{3+} doped C-$CaIn_2O_4$ crystallites

The Eu^{3+} doped C-$CaIn_2O_4$ samples synthesized of inbuilt core–shells of small crystallites of a hybrid structure exhibit multiple phonon bands of the Raman spectrum over 1150–1750 cm^{-1} region. The spectrum is fitted by the Gaussian components in two distinct spectroscopic regions of traditionally so called D-band and G-band of collective oscillations (C=C stretching) of the C-sp^2 rings in a 2D-planar network presumably bonding over the Eu^{3+} doped $CaIn_2O_4$ crystallites. As marked in Fig. 3a in Raman spectrum measured from an as-prepared 1.0 mol% Eu^{3+}:C-$CaIn_2O_4$, the D-band contains two bands at 1185 cm^{-1} and 1310 cm^{-1} in a doublet as shown in a deconvolution (in place of a single symmetric D-band of 1329 cm^{-1} known in a pure grapheme) [23, 24], which reveal two major kinds of a joint C-sp^2 network form and exist on the perpetual Eu^{3+}:$CaIn_2O_4$ facets. As expected, also the G-band is split-up into two overlapping components lying at 1530 and 1650 cm^{-1} (in place of a single G-band of 1591 cm^{-1} known in a pure graphene [23, 24]) in two major kinds of the C-sp^2 network formed in an as-prepared sample. A relative peak intensity $I_D/I_G \sim 0.82$ persists in the D-band over the D-band in this sample. The I_D/I_G ratio describes a figure of merit of an ideal 2D-planar C-sp^2 network. Both the D and G bands reassume 15–45 cm^{-1} of larger frequencies in a reasonably modified spectrum in a self-confined C-sp^2 network on the Eu^{3+}:$CaIn_2O_4$ facets on annealing the sample at 400 °C in air for 2 h in Fig. 3b. During the annealing part of the hot C-sp^2 releases as a gas and the residual reorders in a more rigid and regular network on the facets ($\delta = 1–2$ nm).

Further, the I_D/I_G ration has grown further to 0.96 in account of an induced local microstrain in the conjoint structure, as evident from a large $\gamma = 0.88\%$ value analyzed for the Eu^{3+}:$CaIn_2O_4$ crystallites in terms of inhomogeneous broadening in the XRD peaks in Table 1. Now, let us examine how the D and G bands reorder in frequencies and intensities on annealing the above sample Eu^{3+}:$CaIn_2O_4$ at an effectively higher temperature of 600 °C in air for 2 h, so as an inbuilt C-sp^2 surface layer is thinned down successively to a larger extend of a single molecular level, $\delta \leq 0.5$ nm in Fig. 4a. Despite a reasonably reduced $\gamma = 0.72\%$ value (Table 1), both the D and G phonon bands are promptly converged in further larger frequencies of 1335 cm^{-1} and 1595 cm^{-1} in rather more symmetric and sharp shapes intrinsic of an effectively single molecular GO-network co-bonding in a highly rigid polymer structure on the Eu^{3+}:$CaIn_2O_4$ crystallites via C-O bonds in the oxide polygons. Also, the I_D/I_G ratio is increased to 0.87, conferring a reasonably better C-sp^2 network reordered via C-O moieties on the oxide surfaces. A doublet of two overlapping phonon bands recurring at 460 cm^{-1} and 815 cm^{-1} in Fig. 4b is resolved only when an inbuilt C-sp^2 surface layer had been sufficiently thin down in a 600 °C annealed Eu^{3+}:$CaIn_2O_4$ sample in air. Tentatively,

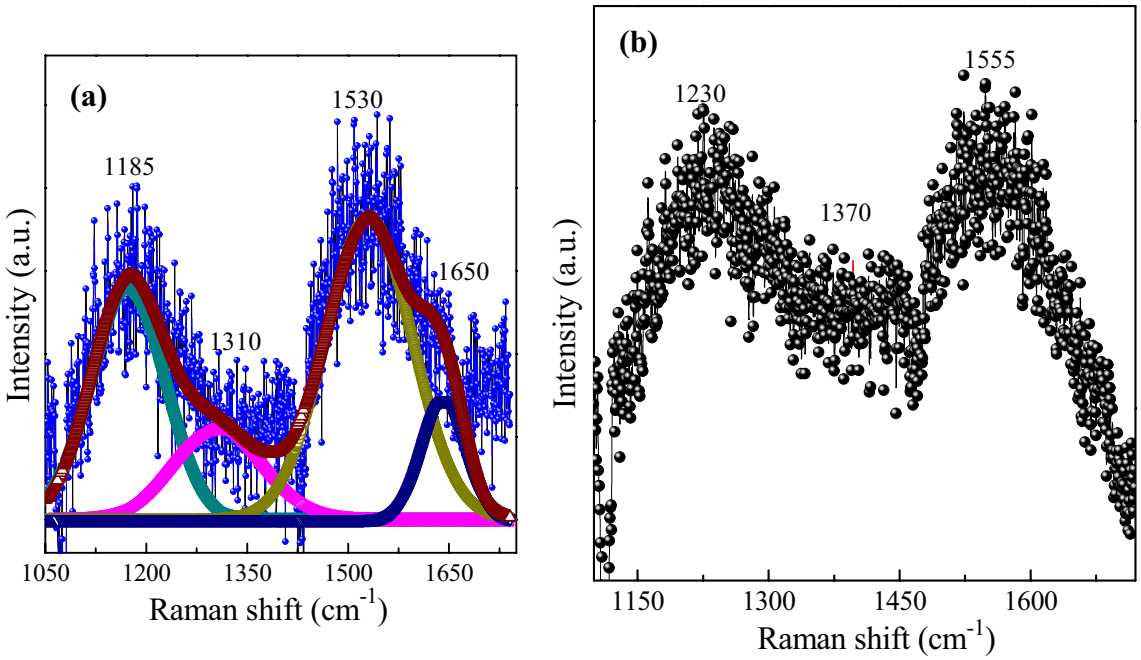

Fig. 3 Deconvoluted Raman bands in a network of a C-sp^2 surface layer in **a** an as-prepared and **b** annealed 1.0 mol% Eu^{3+}:C-$CaIn_2O_4$ sample at (b) 400 °C in air for 2 h

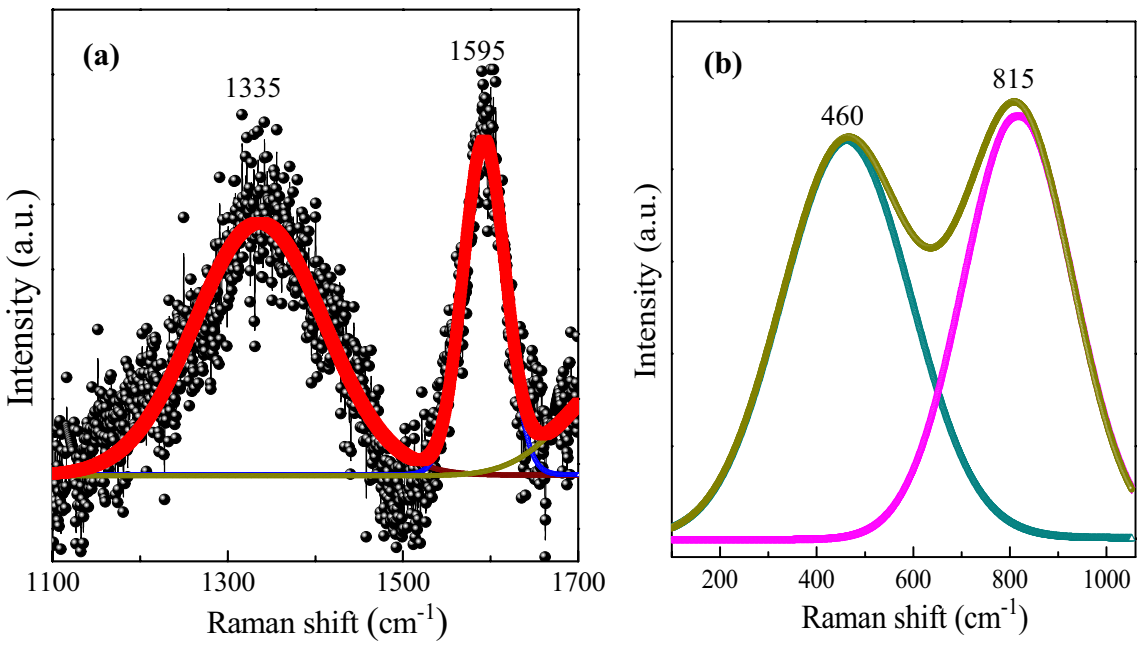

Fig. 4 Raman bands in a network of **a** a conjoint C-sp^2 surface layer and **b** oxide polygons in an annealed 1.0 mol% Eu^{3+}:C-$CaIn_2O_4$ at 600 °C in air for 2 h

the first phonon band of 460 cm^{-1} represents an In-O stretching vibration in a distorted InO_6^{9-} octagon (O_h point group), while the other one of 815 cm^{-1} represents an analogous Ca–O stretching vibration in a distorted CaO_4^{6-} tetragon (T_d point group) in a joint network in a spinel structure [25–28]. These phonon bands are heavily masked in characteristically strong phonon bands recurring in a sufficiently thicker inbuilt C-sp^2 surface layer (shell) on individual Eu^{3+}:$CaIn_2O_4$ crystallites in the other samples processed at lower temperatures. An inbuilt

shell exhibit intense phonon bands in account of a surface enhanced Raman scattering in multiple surfaces in a hybrid core–shell structure. All these results of distribution of phonons unambiguously confirm the fact that the Eu^{3+}:C-$CaIn_2O_4$ samples prepared in a biogenic precursor in this work contain substantially stable inbuilt core–shells of small crystallites.

3.3 XPS bands of Eu^{3+} doped C-$CaIn_2O_4$ crystallites

To find out the chemical state and distribution of the different atoms in a sample Eu^{3+}:C-$CaIn_2O_4$ prepared of small core–shell crystallites, we studied XPS bands in the different atoms in the sample as follows. For example, a Eu^{3+}:C-$CaIn_2O_4$ sample as annealed at 600 °C in air for 2 h exhibits two broad C1s peaks at 288.1 eV and 284.1 eV in Fig. 5a arising in carbon present in C=O (or C–O) and C–C [29, 30] bonds respectively in a presumed GO-like surface layer in the sample of the small crystallites. The C1s band arising from the C=O species has much smaller intensity according to their small numbers present only on the surfaces in a core–shell structure. Figure 5b presents a characteristic doublet of two Ca2$p_{1/2,\ 3/2}$ XPS bands of 345.0 eV and 348.8 eV, with a doublet separation

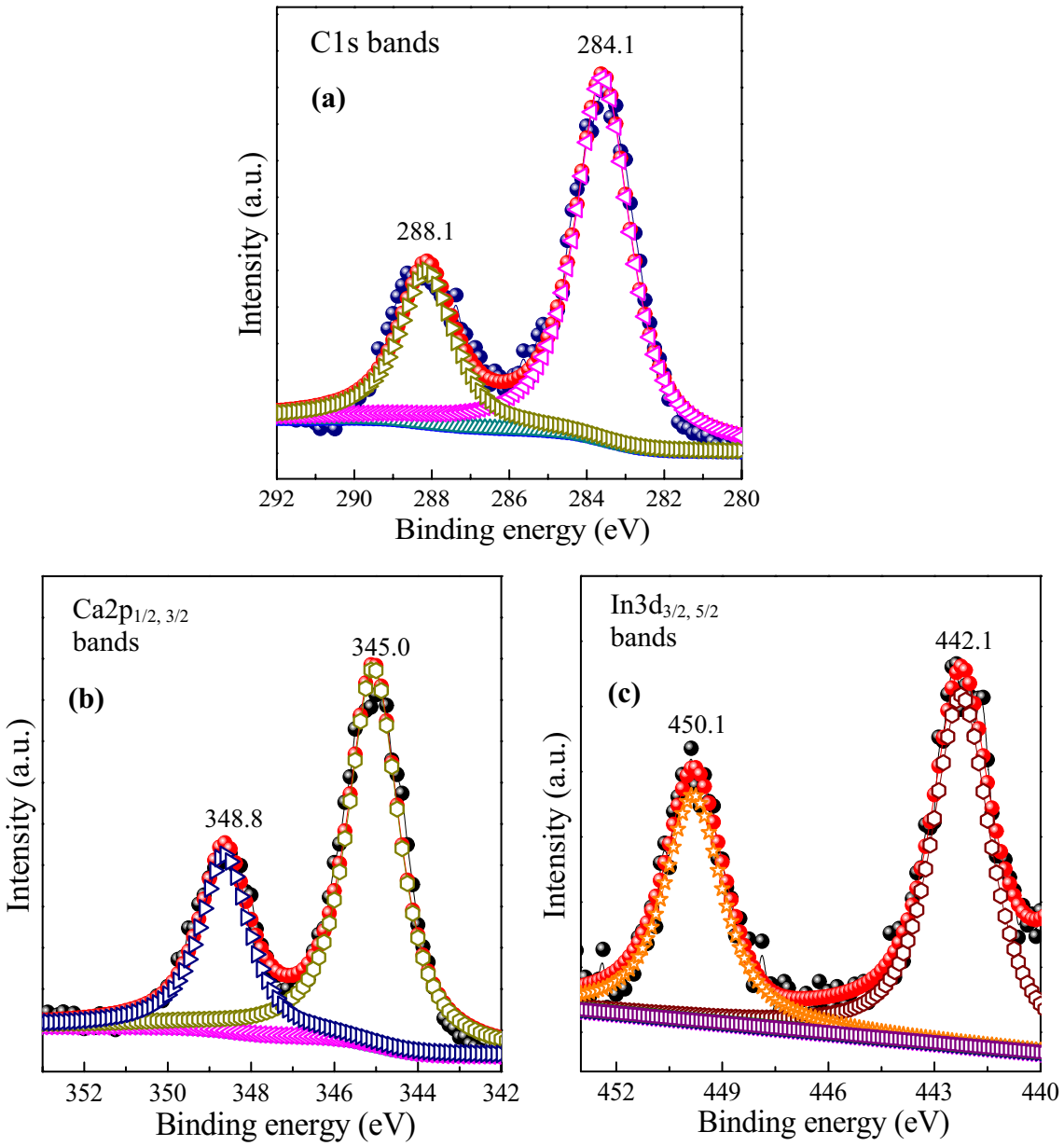

Fig. 5 **a** C1*s*, **b** Ca2$p_{1/2,\ 3/2}$ and **c** In3$d_{3/2,5/2}$XPS bands from a sample of 1.0 mol% Eu^{3+}:C-$CaIn_2O_4$ of small core–shell crystallites (annealed at 600 °C in air for 2 h)

$\Delta = 3.8$ eV, as marked thereby on the respective bands in the Eu^{3+}:C-$CaIn_2O_4$ sample annealed at 600 °C in air for 2 h.

There is no much change in these bands in comparison to those observed before doping $Eu^{3+} \rightarrow In^{3+}$ in a crystal C-$CaIn_2O_4$ lattice. A similar characteristic doublet of XPS bands is observed in In3$d_{5/2}$ and In3$d_{3/2}$ bands at 442.1 eV and 450.1 eV (with $\Delta = 3.8$ eV) in the In^{3+} specifies presumably in the forms of InO_6^{9-} polygons in a Eu^{3+}:C-$CaIn_2O_4$ core–shell structure. Consistently, more or less similar E_b-values have been observed earlier in these Ca2$p_{1/2,\ 3/2}$ and In3$d_{3/2,\ 5/2}$ bands within a small deviation of ± 0.2 eV in solid solutions of In_2O_3-$CaIn_2O_4$ [11] and Eu^{3+}:$CaIn_2O_4$ [31] which were prepared using a conventional high-temperature solid state reaction in ambient air. A marked variation appears in the XPS bands in these species owing to a due change in the local structure especially when mobile O^{2-} vacancies are reordering in a core–shell network structure. The Eu^{3+} species doped in a C-$CaIn_2O_4$ lattice of small crystallites of the above sample share a characteristic doublet of Eu3$d_{5/2}$ and Eu3$d_{3/2}$ bands at 1159.1 eV and 1165.0 eV (with $\Delta = 5.9$ eV) as marked in a deconvolution in Fig. 6a. In a pure Eu_2O_3, these bands appear of bit larger values of 1154 eV and 1163 eV (with $\Delta = 9.0$ eV) in a rather more insulator behavior of $4f^6$-valence electrons [17, 32]. As seen in Fig. 6, XPS bands for europium ion are marked with two bands at 1165 and 1159 eV for Eu^{3+} and Eu^{2+} ions but the band at 1165 eV is 10 times higher in intensity compared to 1159 eV band. So, possibly effect of Eu^{3+} ions are more than Eu^{2+} ions.

Uniquely, the sample reveals three kinds of O^{2-} species, which appear in three overlapping O1*s* XPS bands at 528.9, 529.6 and 530.3 eV in a triplet in a deconvolution of the observed spectrum in Fig. 6b. An undoped sample C-$CaIn_2O_4$ has a strong O1*s* band at 530.3 eV with only a weak shoulder at 531.8 eV, illustrating that a $Eu^{3+} \rightarrow In^{3+}$ doping significantly modifies a distribution of density of states of O^{2-} electrons in the different sites in a Eu^{3+} doped C-$CaIn_2O_4$ of small crystallites. Qualitatively, the first two bands observed at 528.9 eV and 529.6 eV in strong intensities attribute to O^{2-} species occupying the two kinds of the oxide polygons of CaO_4^{6-} and InO_6^{9-} respectively as per their ratio 1:2 in a spinel $CaIn_2O_4$ structure. Thus, a weak satellite band observed at 530.3 eV (or 531.8 eV in the undoped sample) can be assigned to the surface O^{2-} species present as functionalized groups, like C=O, C–O, or CHO [33–35], in a conjoint C-sp^2 surface layer of a stable network on the individual crystallites in a hybrid core–shell structure. It is a hybrid core–shell structure that finely tunes the E_b values and intensities in the three distinct overlapping O1*s* bands in a wide O1*s* distribution of electrons in the different sites in the lattice in this example.

Now, let us comment on how a thermal annealing leads to tailor characteristic (A) In3$d_{3/2,5/2}$, (B) O1*s*, and (C) C1*s* XPS bands at the expense of an inbuilt C-sp^2 surface layer (shell) in a typical 1.0 mol% Eu^{3+} doped sample C-$CaIn_2O_4$ of small crystallites of a tailored core–shell structure. As a result, Fig. 7 compares the three band groups of A, B, and C observed in (a) the as-prepared and annealed samples at (b) 400 °C and (c) 600 °C for 2 h in air in a way the shell thins down in successive layers {from an average $\delta = 2$–3 nm thickness in the beginning sample (a) to a single molecular level $\delta \rightarrow 0.5$ nm or smaller in sample (c)}

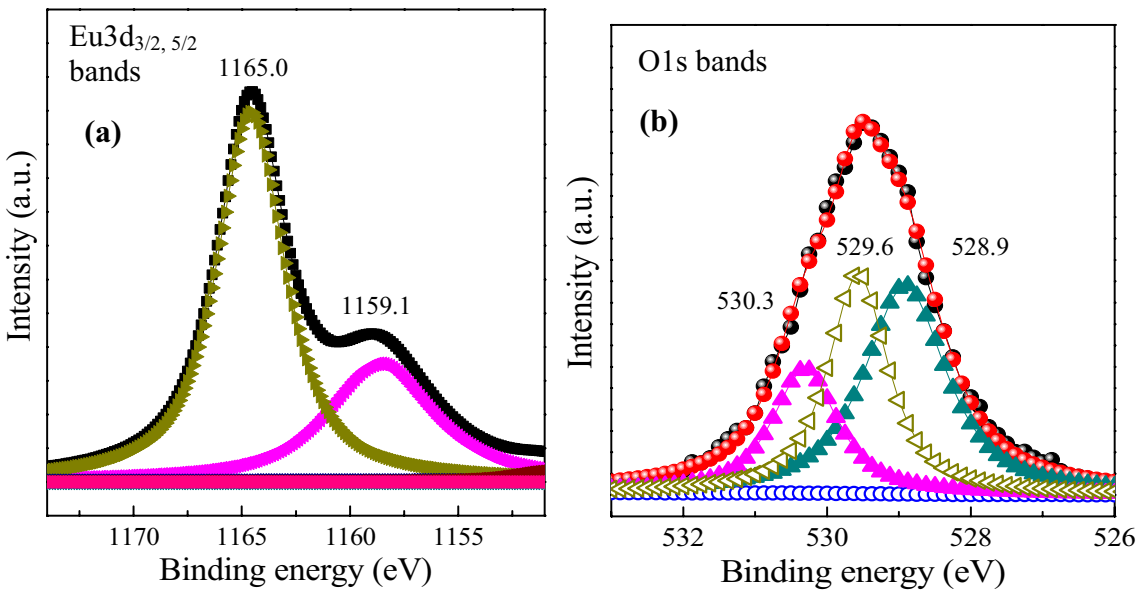

Fig. 6 **a** Eu3$d_{3/2,5/2}$ and **b** O1*s* XPS bands from a sample of 1.0% Eu^{3+}:C-$CaIn_2O_4$ of small core–shell crystallites (annealed at 600 °C in air for 2 h)

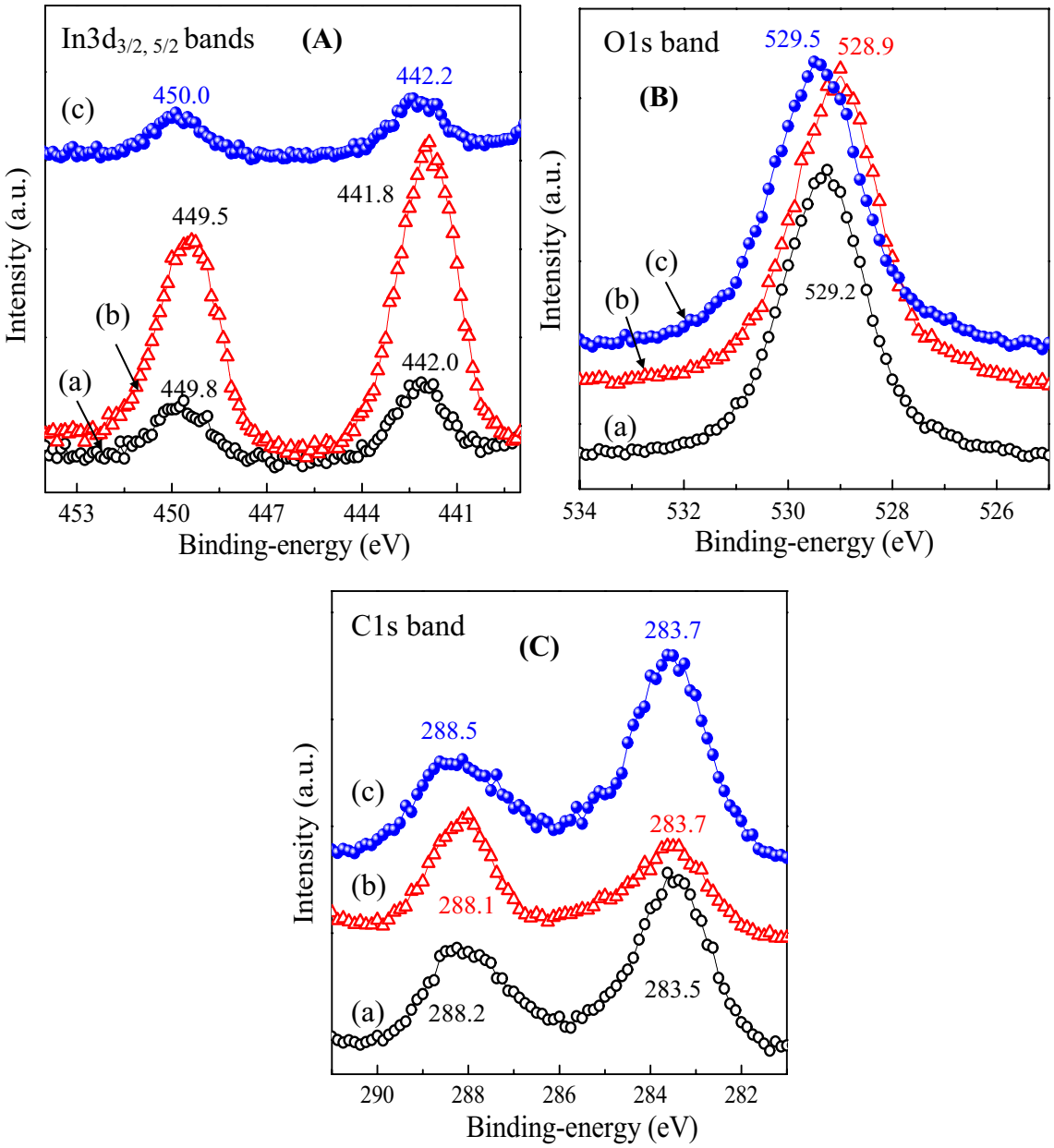

Fig. 7 **A** In3$d_{3/2,5/2}$, **B** O1*s*, and **C** C1*s* XPS bands measured from (a) as-prepared and annealed 1.0 mol% Eu^{3+}:C-$CaIn_2O_4$ at (b) 400 °C and (c) 600 °C for 2 h in air

in progressively tuned core–shell crystallites. Peculiarly, the In3$d_{3/2,5/2}$ bands are sharpened (over bit smaller E_b values) in account of a reasonably manifested intensity in an optimally 400 °C annealed sample and then they lose intensity in diffuse bands of significantly promoted E_b—value by nearly 0.5 eV in a critically 600 °C annealed sample. Also the O1*s* band assumes a minimum 528.9 eV value in this sample relative to that of 529.2 eV in the as-prepared, or 529.5 eV in a 600 °C annealed sample in a marked reordering of O^{2-} species in the shell and surface-interfaces in a hybrid core–shell structure. Also, the C1*s* band component (band-1) lying of a lower E_b-value at 283.7 eV readapts a markedly reduced intensity compared to its higher E_b-value component (band-2) at 288.1 eV in an optimally 400 °C annealed sample. The result accords with a reasonably increased number density of C–C and C=C bonds (band-1) reformed in a top surface layer in a C-$CaIn_2O_4$ core shell at the expense of the functional C–O, C=O, CHO groups in a 600 °C annealed sample. Further, diffuse In3$d_{3/2,5/2}$ XPS bands observed in Fig. 7A in a 600 °C annealed Eu^{3+}:C-$CaIn_2O_4$ sample illustrate a disordering of InO_6^{9-} polygons on the In^{3+} cations on the surfaces in the

small crystallites. This is a very similar observation as that we described in ACS SC&E research paper [19] in critically hot InO_6^{9-} polygons refine into tripods 'InO_3', which co-bond one another in a more stable 2D-network involving C-sp^2, C–O and C=O species in different ways at the surfaces in a disordered structure. At an elevated temperature, a regular network of the hot C-sp^2 species dissociates to release highly reactive C-sp^2, part of which reacts with the 'InO_3' tripods, creating an 'alloyed In_2O_3–C surface' on the nascent $CaIn_2O_4$ facets. That is what it appears in diffuse characteristic In3$d_{3/2,5/2}$ XPS bands as observed over here in a critically annealed sample of Eu^{3+} doped C-$CaIn_2O_4$ at 600 °C for 2 h in air. It is useful to fruitfully tailor the local core–shell structure and in turn the useful functional properties as will be described further.

3.4 Microstructures of Eu^{3+} doped C-$CaIn_2O_4$ crystallites

The size, shape and surface morphology in as-prepared and annealed samples Eu^{3+}:C-$CaIn_2O_4$ of small crystallites, prepared with Eu^{3+} contents varied in small dosages of 0.5, 1.0, 1.5 and 2.0 mol%, can be analyzed in terms of their FESEM and HRTEM images studied at selective magnifications. The results help to find out the mechanism in a sample of small core–shell crystallites refines on the optimal annealing in a hierarchical structure via a residual carbon of a thin C-sp^2 microscopic layer in a hybrid structure. The FESEM images present mostly thin plates of the Eu^{3+}:C-$CaIn_2O_4$ sample of tiny crystallites binding one another in small groups in a hierarchical structure, with 100–150 nm widths and 20–40 nm thickness (which represents the effective crystallite size). This is a characteristic feature of the small crystallites are cross-linked via the C-sp^2 surface in this specific structure. An aloe-vera gel used as a precursor medium in synthesizing the sample is found to be highly efficient in controlling the final size, shape and morphology in the small Eu^{3+}:C-$CaIn_2O_4$ crystallites. Distinct plates of the Eu^{3+}:C-$CaIn_2O_4$ crystallites grown preferentially in the (200) planes as illustrated with XRD patterns has been published in MRS Advances in 2017 can be observed in the HRTEM images at a reasonably higher magnification [36]. A SAED pattern taken from a thin plate grown in (200) planes of HRTEM images revealed arrays of the lattice points. The (200) arrays are marked at $d_{200} = 0.3050$ nm in agreement with the XRD value. An inbuilt C-sp^2 surface layer shares a broad diffraction halo of a ring (near the center) in its characteristic (002) arrays in a graphene like network structure of hexagonal rings with $d_{002} = 0.3460$ nm [19]. The result confers that the plate in the observation does contain an inbuilt surface layer of a core–shell crystallite. These images are clearly bound by a conjoined peripheral surface layer (of distinct darkish contrast), showing the plate, which is grown in (200) facets, contains a bonded C-sp^2 surface over layer, what is it is marked over its left top corner. The results characterize the sample Eu^{3+}:C-$CaIn_2O_4$ forms a hybrid composite structure of small core–shell crystallites. A core shell Eu^{3+}:C-$CaIn_2O_4$ structure and its hierarchical composite structure bonding through a conjoint C-sp^2 surface layer distinctly vary in an annealed sample at 400–600 °C for 1–2 h in air. This is clearly observed in FESEM and HRTEM images studied in the annealed samples. For example, Fig. 8a, b presents FESEM and HRTEM images of a sample 1.0 mol% Eu^{3+}:C-$CaIn_2O_4$ annealed at 400 °C for 2 h in air. Thin plates of core–shell crystallites as observed in an as-prepared sample are grown into a hierarchical structure in a shape laminates, with 500–1000 nm widths and 30–50 nm thickness (represents the average crystallite size), in the FESEM images in Fig. 8a.

Small plates Eu^{3+}:C-$CaIn_2O_4$ embedding in a carbon film are also observed in HRTEM images in Fig. 8b as measured from the same sample. Figure 8c displays lattice images of (004) planes of a thin plate of HRTEM images in Fig. 8b, with a d_{004}-spacing of 0.2568 nm). A thin crystal plate grown in (200) planes, as observed in the HRTEM images in Fig. 8b, displays a SAED pattern of regular arrays of the lattice points in two different series of (004) and (112) planes as shown in Fig. 8d. The lattice separations of $d_{004} = 0.2568$ nm and $d_{112} = 0.3295$ nm observed in these arrays fairy reproduce the corresponding values observed in the XRD peaks of 0.2568 nm and 0.3310 nm in this sample. As observed in the as-prepared sample, a presumed inbuilt C-sp^2 surface layer of a hexagonal network is sharing a characteristic broad diffraction halo of a circular ring (near the centre) in its characteristic (002) arrays, with a modified $d_{002} = 0.3455$ nm,[7] as on it presumably confining in a thinner conjoin shell in the crystallites. Figure 9 displays a very complicated hierarchical structure of pretty long thin flakes of FESEM (1–2 μm widths and 25–35 nm thickness), which were grown in support of presumably long surfaces of the biogenic templates as used in the synthesis, in a 2 mol% Eu^{3+}:C-$CaIn_2O_4$ sample annealed at 400 °C for 2 h in air.

A refined C-sp^2 surface layer on the crystallites (in a shape of thin plates) promptly cross-links the bare crystallites in this specific structure of a hybrid composite. A similar microstructure prevails on raising the $Eu^{3+} \rightarrow In^{3+}$ doping further in a sample 2.0 mol% Eu^{3+}:C-$CaIn_2O_4$ studied in this series. Nevertheless, presumably small plates of small crystallites can be resolved in these samples only after etching out most of the C-sp^2 surface layers in critically annealed samples in air. For example, Fig. 10a, b presents a rather clear picture of thin flakes or plates of the crystallites in the Eu^{3+}:C-$CaIn_2O_4$ samples (having 1–2 mol% $Eu^{3+} \rightarrow In^{3+}$ doping, so as it effectively promoting growth

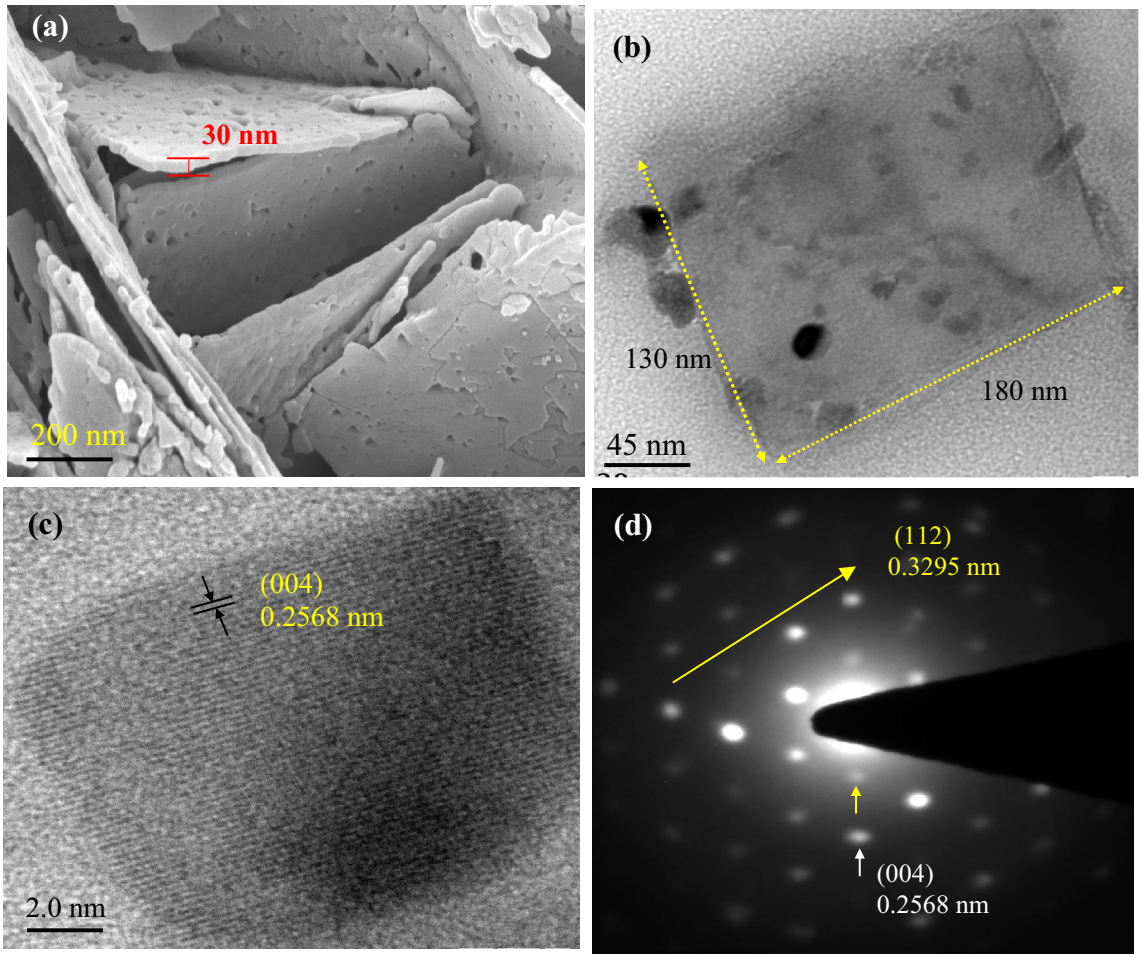

Fig. 8 **a** FESEM, **b** HRTEM, **c** lattice image, and **d** SAED pattern from a 1.0 mol% Eu^{3+}:C-$CaIn_2O_4$ sample of small crystallites annealed at 400 °C for 2 h in air

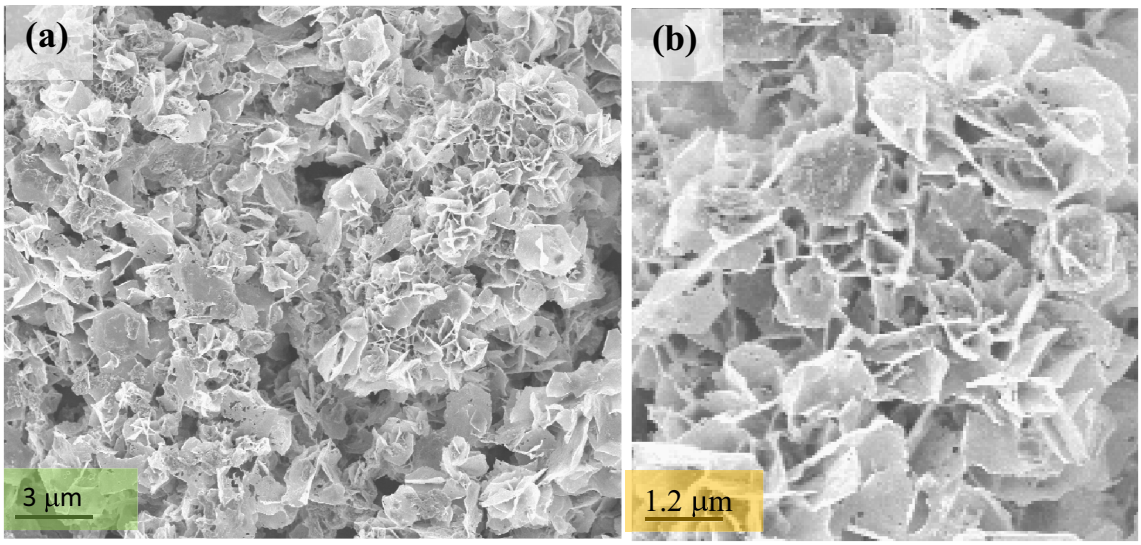

Fig. 9 **a**, **b** FESEM images of a 2 mol% Eu^{3+} doped C-$CaIn_2O_4$ sample (annealed at 400 °C for 2 h in air) grown as thin platelets as magnified in **b**

of the crystallites over larger exposed facets) optimally annealed at 600 °C for 2 h in air. Bare crystallites grown in a specific shape of rectangular prisms with well-developed facets (200) and (112) facets are observed in Fig. 10b, c in a sample 2.0 mol% Eu^{3+}:C-$CaIn_2O_4$ annealed at 600 °C for 2 h in air. Well-separated prisms are 50–100 nm long, with W = 25–50 nm widths and δ = 25–40 nm thicknesses. The model shapes of these crystallites are given in Fig. 10d

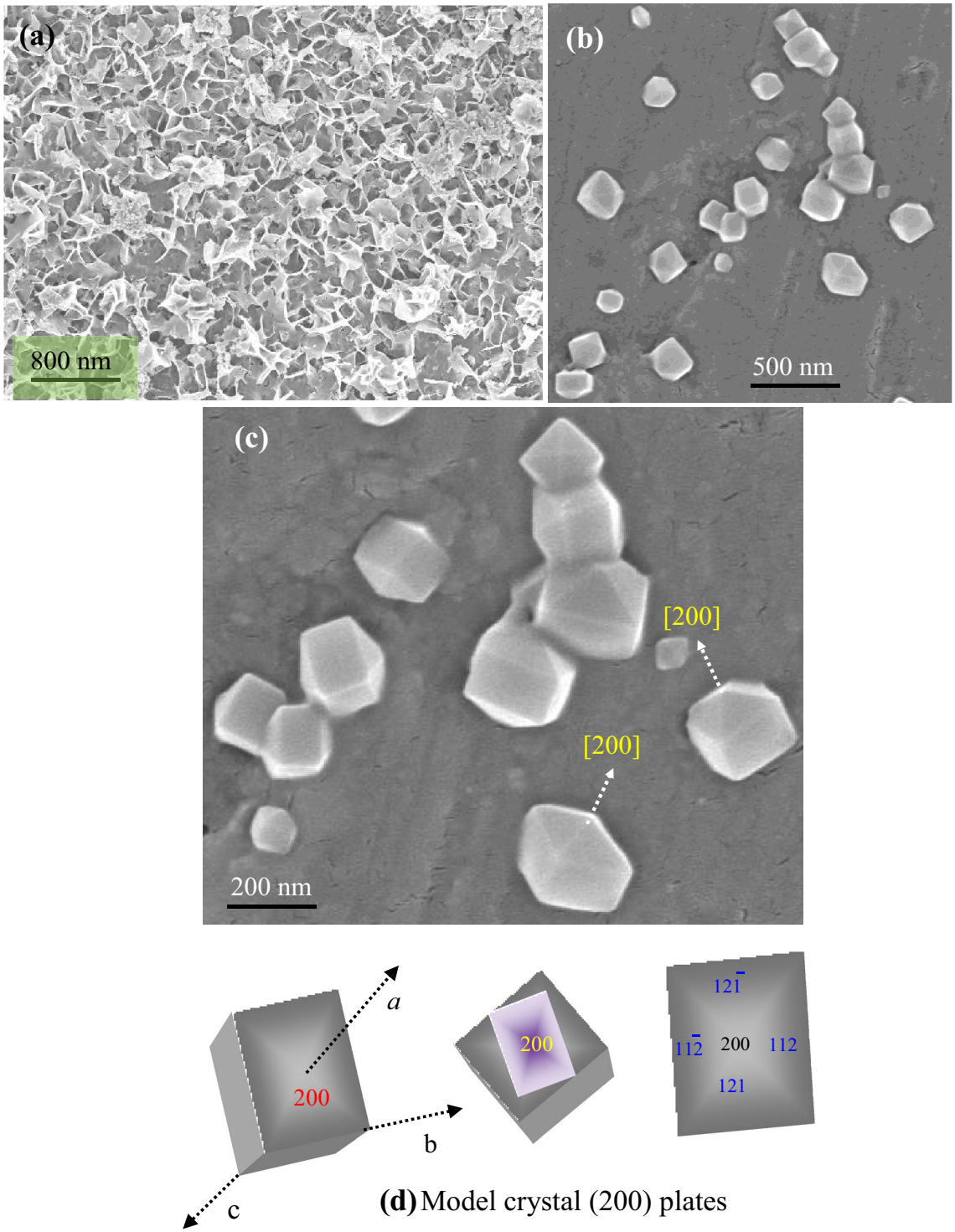

Fig. 10 FESEM images of **a** 1.0 mol% and **b**, **c** 2.0 mol% Eu^{3+} doped C-$CaIn_2O_4$ grown in thin **a** plates and **b**, **c** rectangular prisms as annealed at 600 C for 2 h in air, with **d** the model crystal plates grown with distinct facets

illustrating how the small crystallites are grown in the perpetual facets. It is interesting to observe that, also the single crystallites are shown to be cross-linking (via O^{2-} in the oxide polygons at reactive facets in a $CaIn_2O_4$ lattice) one over others in a 'second level hierarchical structure'. Now, let us view HRTEM images in Fig. 11a from a typical 2.0 mol% Eu^{3+}:C-$CaIn_2O_4$ sample annealed at 600 °C for 2 h in air., wherein the small crystallites are binding one another via the inbuilt C-sp^2 surface layers ($\delta \leq 0.5$ nm) in self-assemblies of a 'hierarchical structure'. A typical lattice image measured from a selected plate A (as marked in the HRTEM images in Fig. 11a) in Fig. 11b reveals how it is preferentially grown in a single crystallite in (200) planes, with $d_{002} = 0.3060$ nm (consistent to a corresponding value

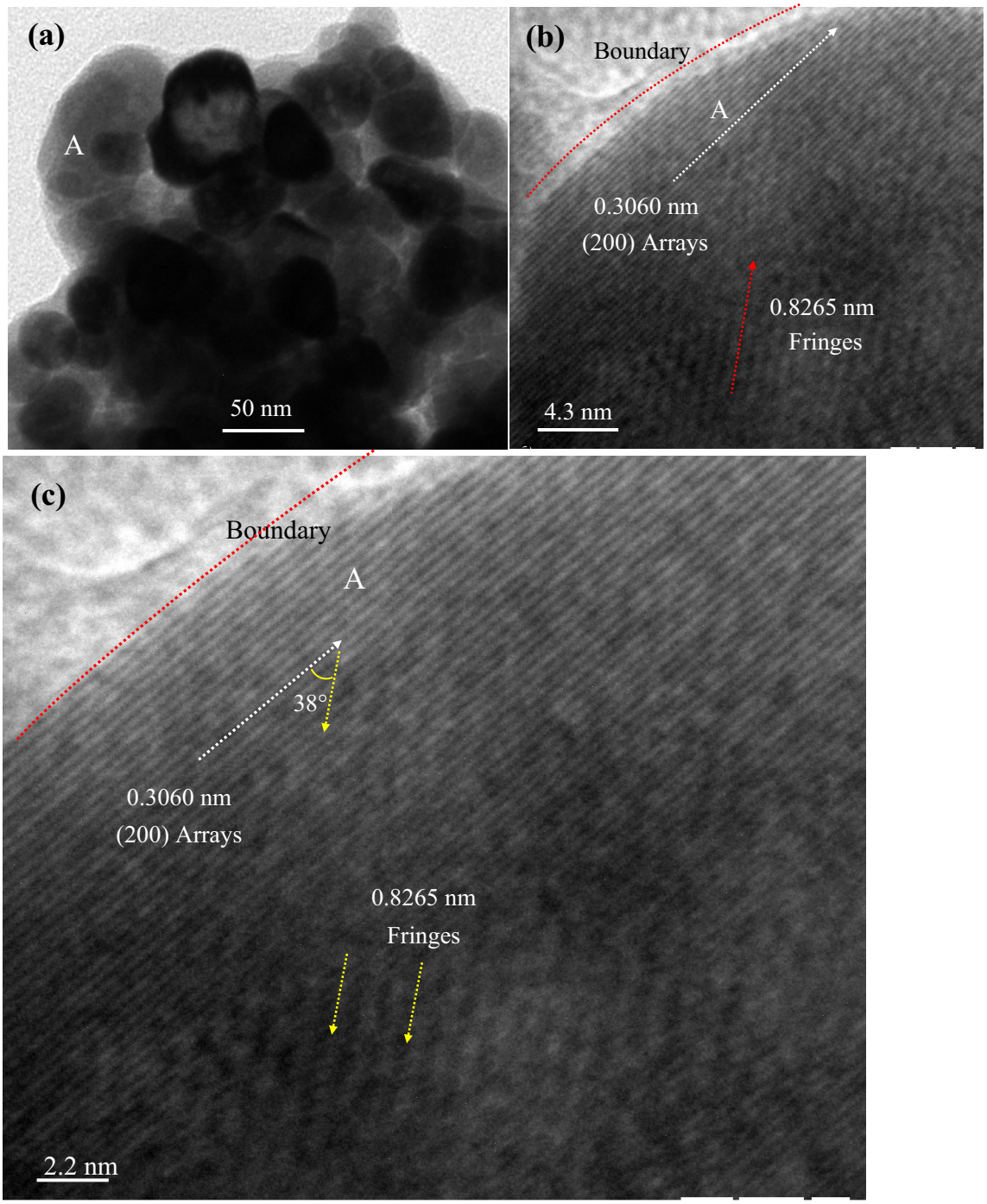

Fig. 11 HRTEM images of **a** thin crystal plates bonding over an inbuilt C-sp^2 surface layer and **b**, **c** lattice patterns from a 2.0 mol% Eu^{3+} doped C-$CaIn_2O_4$ sample (annealed at 600 °C for 2 h in air). Interference fringes from an inbuilt surface layer on a plate are shown

of 0.3062 nm observed in the XRD pattern), and how it contains a distinct peripheral boundary (of a whitish contrast) in part of a bonded surface layer. As magnified in Fig. 11c, it exhibits a large number of linear interference fringes of an internal separation of 0.8265 nm (which is much larger than expected d_{hkl} in this sample) in interference of the electron beams reflected from successive C-sp^2 layers on a perpetual crystal facet. Eventually, the interference fringes are intersecting the lattice arrays at a specific internal angel of 38°, which is nearly the same throughout the observed fringes.

Figure 12a presents another example of a lattice image taken from one of the single crystallites grown in a self-assembly as marked in region 'A' in Fig. 11a. As marked by numbers 1, 2, 3 and 4, this crystallite contains a distinct phase boundary of a conjoint surface layer (of a disordered phase) formed on its multifacets, which eventually appear in four distinct microscopic regimes, likely from four conjoint facets in this crystallite. Uniquely, all the four facets share a uniform thickness of an inbuilt conjoint surface layer, $\delta \sim 0.7$ nm, in a regular molecular structure at an atomic scale, accounting in a continuous interconnected C-sp^2 network forms over a crystallite in minimizing the total surface-energy in a hybrid core–shell structure. The said crystallite in this example (a 2.0 mol% Eu^{3+} doped C-$CaIn_2O_4$ sample and annealed at 600 °C for 2 h in air in thinning down a surface layer in a critical core–shell structure) reveals regular (112) arrays of lattice images, with $d_{112} = 0.3325$ nm (consistent to its value shown in the XRD peak at 0.3310 nm) as studied using an electron beam incident on its (112) facet. As magnified in Fig. 12b, it exhibits a wide series of linear interference fringes of an internal separation of 0.8065 nm and an average 0.51 nm fringe-width when the indent electron beam reflecting from successive C-sp^2 surface layers on the (112) facet in a way the later get a conjoint constructive interference in an ordered pattern.

Eventually, these fringes are inclined uniformly over the (112) lattice arrays at a specific internal angel of 41°, which does not change noticeably over the entire range of the observed fringes. Further, these fringes have an average width of 0.51 nm, which is nearly the same as observed above in Fig. 12b in a similar pattern of the interference fringes formed on a (200) crystal facet in a similar preferentially grown single crystallite in the (200) planes. A fringe width observed in this experiment seems to be critical of a conjoint C-sp^2 network (in terms of its thickness and molecular structure) formed on the sample of its bare surfaces. These are general microscopic features in unambiguously characterizing a core–shell structure of metals, metal oxides, and derived structures. A spatial distribution of the atoms in a Eu^{3+}:C-$CaIn_2O_4$ hybrid nanostructure was studied in terms of its characteristic elemental mapping of selected regions of the FESEM images with an in situ EDX analysis, which evaluates the Eu, C, Ca, In and O species in the chosen microscopic regions. As shown in the typical spectra in Fig. 13, all the four kinds of atoms are duly distributed in a due distribution in a 1.0 mol% Eu^{3+}:C-$CaIn_2O_4$ sample, as-prepared in a self-combustion of a biogenic complex in air. For a comparison at a glance, the different

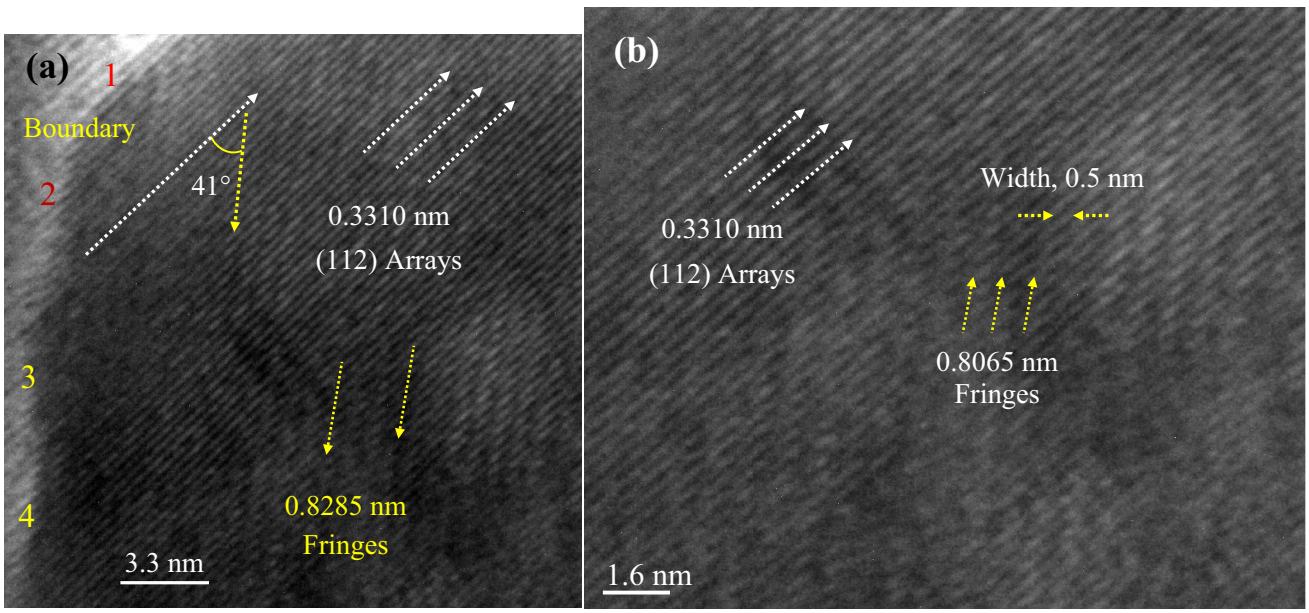

Fig. 12 **a** Lattice images from a 2.0 mol% Eu^{3+}:C-$CaIn_2O_4$ sample of a single crystal plate grown in (112) facets (annealed at 600 °C for 2 h in air), with **b** a magnified view containing interference fringes. A boundary phase extends over four segments 1 → 4

elements are given in different colors; white for Eu, red for C, green for Ca, blue for In, and yellow for O. Similar results were obtained for all other samples studied in this work. As expected, an initial C-content has been progressively reduced in optimally annealed samples at 400–600 °C for 1–2 h in air.

4 Tailored optical properties of Eu^{3+} doped C-$CaIn_2O_4$ crystallites

Figure 14 shows absorption spectra of annealed Eu^{3+}:C-$CaIn_2O_4$ samples at 400 °C for 2 h in air, containing (a) 0.1, (b) 0.5, (c) 1.0 and (d) 2.0 mol% Eu^{3+} doages. The primary band-1, which is observed at 205 nm (215 nm before the annealing) [35] in Fig. 14a in a sample doped by only 0.1 mol% Eu^{3+}, is shifted progressively over lower λ-values below 200 nm and only its tail extends over longer λ-values above 200 nm in a distinct band edge absorption. Uniquely, a weak absorption band is developed in the visible region at 645 nm in a $^7F_3 \rightarrow {}^5D_0$ transition from the Eu^{3+} ions in Fig. 14c after a critical 1.0 mol% Eu^{3+} doping in C-$CaIn_2O_4$ in a core–shell structure. Another weak band is developed in the visible region at 785 nm (in a $^7F_6 \rightarrow {}^5D_0$ transition [15, 36, 37] of the Eu^{3+} ions) in Fig. 14a after a rather smaller doping of only 0.1 mol% Eu^{3+} in a core–shell C-$CaIn_2O_4$ structure. Both these bands were not so visible before thermal annealing the sample in a marked effect of the annealing in which a significant part of the Eu^{3+} ions presumably segregates from the lattice (core) and migrates to the interfaces (shell) in a refined hybrid core–shell structure. Eventually, both of the bands

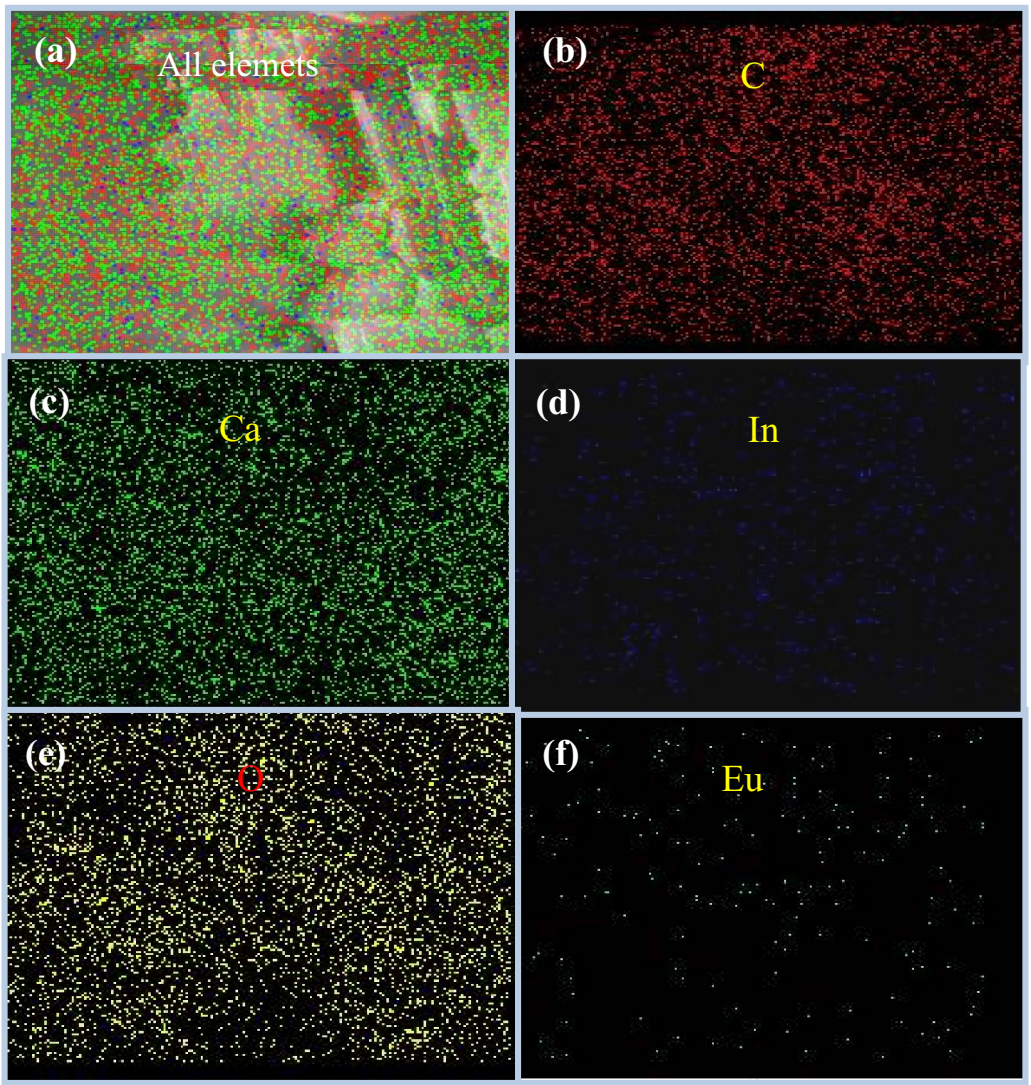

Fig. 13 The elemental mapping of an as-prepared 1.0 mol% Eu^{3+}:C-$CaIn_2O_4$ hybrid nanostructure; **a** all the different elements shown together and the individual ones **b** C, **c** Ca, **d** In, **e** O and **f** Eu marked in the different visible colors

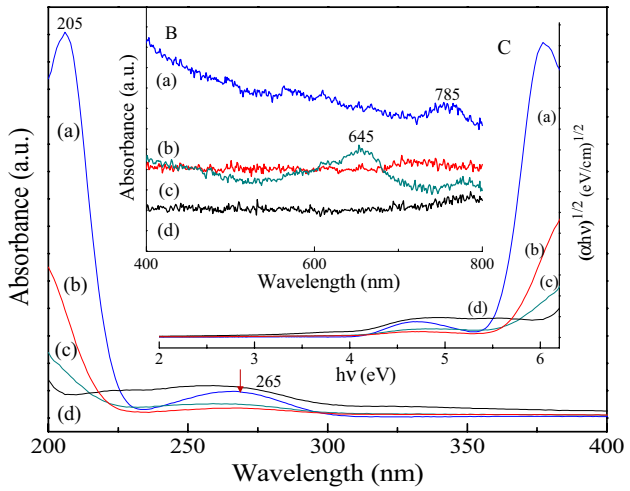

Fig. 14 **A** UV–visible absorption spectra of annealed Eu^{3+}:C-$CaIn_2O_4$ at 400 °C, with (a) 0.1, (b) 0.5, (c) 1.0, and (d) 2.0 mol% Eu^{3+} dosages, **B** part of magnified spectra over 400–800 nm, and **C** Tauc plots of tail of band-1 over lower energies

Table 2 Optical parameters derived from light absorption spectra in Eu^{3+}:C-$CaIn_2O_4$ of small core shell crystallites dispersed in water

Eu^{3+}:C-$CaIn_2O_4$	λ_{max} (nm)	ε_{max} ($M^{-1}Lcm^{-1}$)	E_g (eV)
As-prepared			
0.1[a]	219	8.0×10^4	5.01
0.5[a]	218	7.3×10^4	5.21
1.0[a]	217	6.7×10^4	5.30
2.0[a]	207, 265	5.4×10^4, 0.6×10^4	5.41
Annealed 400 °C, 2 h			
0.1[a]	205, 265	4.7×10^4, 0.3×10^4	5.30
0.5[a]	202	1.7×10^4	5.40
1.0[a]	200	0.7×10^4	5.61
2.0[a]	195, 265	0.4×10^4, 0.4×10^4	5.41
Annealed 600 °C, 2 h			
0.1.0[a]	216	6.8×10^4	5.21
0.5[a]	210, 265	5.7×10^4, 1.7×10^3	5.42
1.0[a]	190	0.3×10^4	5.92
2.0[a]	195, 268	0.7×10^4, 0.5×10^4	5.31

[a]The Eu^{3+}-dosages in mol%

are the hot bands, which can be excited only in the high-energy carriers of occupied sites in the interfaces in a firmly stable core–shell structure [1, 2, 17].

As usual, the Tauc plots of the tail in absorption band-1 over lower energies are used in estimating the E_g-values from the spectra given in Fig. 14 from four annealed samples Eu^{3+}:C-$CaIn_2O_4$ at 400 °C for 2 h in air. The values of λ_{max}, extinction coefficient (ε_{max}) and E_g obtained from absorption spectra in the different the as-prepared and annealed Eu^{3+}:C-$CaIn_2O_4$ samples are given in Table 2. Further, as compiled in Fig. 15, the present light absorption spectra were further modified in the samples Eu^{3+}:C-$CaIn_2O_4$ were annealed at an effectively higher temperature of 600 °C for 2 h in air. Here, band-1 is markedly broadened in samples (a, b), while the band-2 is grown in a more pronounced band with its average position lying at 265 nm, which does not exhibit a measurable in the as prepared and annealed sample at 400 °C for 2 h in air. Obviously, it is the result of a presumably refined grafted C-sp^2 surface layer reformed on the facets of small core–shell Eu^{3+}:$CaIn_2O_4$ crystallites. An energy-transfer $Eu^{3+} \rightarrow$ C-sp^2 thus accounts in an enhanced intensity in the $\pi \rightarrow \pi^*$ transition in excited C-sp^2 species in a rigid core-shell. These samples have bit lowered E_g-values (as given in Table 2) than those having more Eu^{3+} species, which help mixing in the closely lying energy levels involved between the two types of the species in a joint 2D-network in this example.

As usual, characteristically weak absorption bands expected in the spin-forbidden $4f \rightarrow 4f$ transitions of $Eu^{3+}(4f^6)$ ions [38] are masked in the strong background absorption from a due band edge absorption tail (of a strongly electric-diploe-allowed transition) in a result of the excitation of the charge carriers from the valence band to the condition band in a hybrid core-shell Eu^{3+}:C-$CaIn_2O_4$ structure. Such microscopic structure has large multiple surfaces of core, interface, top network layer that all share strong recurring surface scattering throughout the spectral region over 200–800 nm studied in this example. Nevertheless, the Eu^{3+}–energy levels present in this spectral region exhibit strong surface enhanced light-emission. Technically, it is very useful that the Eu^{3+} ions doped in a

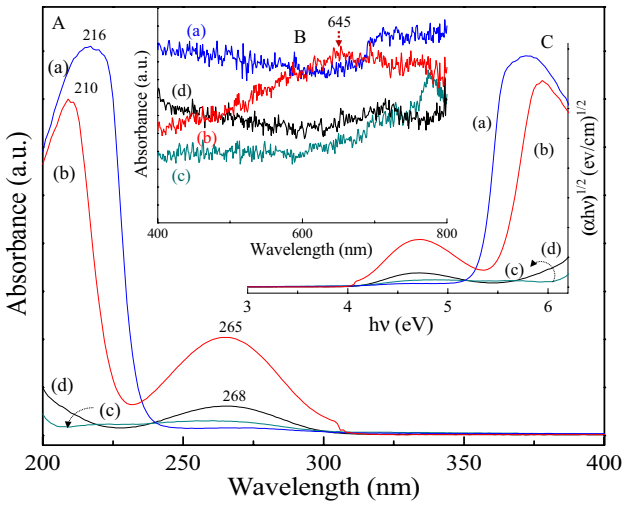

Fig. 15 **A** UV–visible absorption spectra of Eu^{3+}:C-$CaIn_2O_4$ annealed at 600 °C for 2 h in air, with (a) 0.1, (b) 0.5, (c) 1.0, and (d) 2.0 mol% Eu^{3+} dosages, **B** part of magnified spectra over 400–800 nm, and **C** Tauc plots band-1 over lower energies

host C-$CaIn_2O_4$ of a core structure of the small crystallites exhibit strong light-emission of a broad spectrum over the UV–visible regions. For example, Fig. 16 compares (A) light emission and (B) excitation spectra for the samples (as-prepared) having (a) 0.1, (b) 0.5, (c) 1.0, and (d) 2.0 mol% Eu^{3+} dosages, as on measured using a pulse xenon lamp of a light source. The emission spectra were obtained by exciting the samples at $\lambda_{ex} = 240$ nm, while the excitation spectra were obtained by irradiating the samples in the emission band at $\lambda_{em} = 512$ nm in finding the optical origin of electronic transitions in these bands. In general, two broad groups of emission appear over (1) 300–580 nm and (2) 580–900 nm on exciting the samples at a common $\lambda_{ex} = 240$ nm, while those of the excitation spectra appear in a strong group in the far UV region over 210–310 nm with rather weak bands extending over longer wavelengths 310–430 nm on a common $\lambda_{em} = 512$ nm irradiation by the xenon lamp.

On the basis of light-emission reported in Eu^{3+} ions doped in different optical hosts [31], the blue light-emission of average peak position lying around 435 nm ascribes to the $^5D_3 \rightarrow {}^7F_0$ transitions, while the red emission of average peak position lying around 660 nm ascribes to the $^5D_0 \rightarrow {}^7F_4$ transitions of the Eu^{3+} ions in the $CaIn_2O_4$ lattice. A strong excitation band prevails below 240 nm due a prominent metal-to-ligand $Eu^{3+} \rightarrow O^{2-}$ charge-transfer [1, 37] in the small Eu^{3+}:C-$CaIn_2O_4$ crystallites. This charge transfer is between europium ions and oxygen ions present in indium oxide polygons in interstitial sites. As stated in this research that the reordering of indium oxide polygons is taking place on annealing, lastly it's a mixed structure ($CaIn_2O_4$) with few oxygen vacancies. The 4*f*–4*f* electronic energy-levels of $Eu^{3+}(4f^6)$ ions, which share the light-emission and excitation spectra in these samples are given in the insets in Fig. 16. Eventually, the Eu^{3+} ions exhibit a series of emission and excitation bands extending over the entire UV–visible regions what is it is a great demand nowadays in finely tuning the light absorption, emission and associated properties in a kind of a hybrid nanocomposite of small core–shell crystallites.

Both the excitation and emission spectra in Fig. 16 had acquired a maximum intensity in a critical dosage of 0.5 mol% Eu^{3+} ions, i.e., the concentration quenching (Q_c), in the as-prepared Eu^{3+}:C-$CaIn_2O_4$ samples. A similar $Q_c \sim 1.0$ mol% Eu^{3+} value has been reported in Eu^{3+}:Y_2O_3, while an order of lower value is reported in Eu^{3+}:C-$CaIn_2O_4$, which were prepared in pretty bigger crystallites by heating the precursors at an effectively higher temperature 1000 °C for 3 h in air [31]. Now, let examine how the light emission and excitation spectra change on a core–shell structure is finely modified in the annealed Eu^{3+}:C-$CaIn_2O_4$ samples. Figure 17 compares light-emission spectra obtained for the samples (annealed at 400 °C for 2 h in air) under identical to those reported in Fig. 1. An obviously effect of an annealing is that it induced an higher-energy emission $^5D_4 \rightarrow {}^7F_0$ displaced at 355 nm and a long wavelength $^5D_0 \rightarrow {}^7F_4$ red-emission at 695 nm as marked on the individual bands. A maximum light-emission is retained in the same sample as that it contains 0.5 mol% Eu^{3+} before the annealing. Involved energy-levels in these spectra are given in the insets in Fig. 17. As can be seen

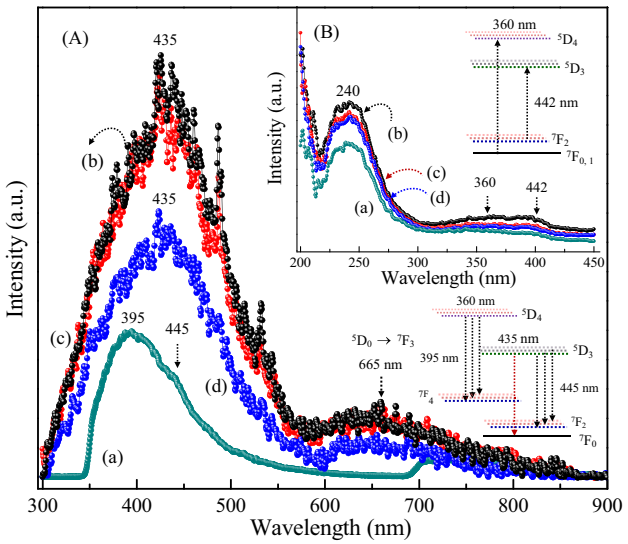

Fig. 16 **A** Light-emission ($\lambda_{ex} = 240$ nm) and **B** excitation spectra ($\lambda_{em} = 512$ nm) measured from Eu^{3+}:C-$CaIn_2O_4$ core–shell crystallites (as-prepared); (a) 0.1, (b) 0.5, (c) 1.0, and (d) 2.0 mol% Eu^{3+}-doping dosages, with associated energy-levels in the insets

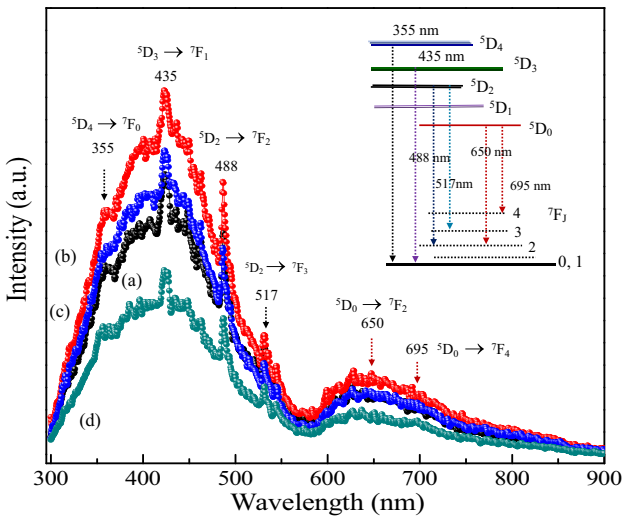

Fig. 17 Light-emission ($\lambda_{ex} = 240$ nm) in thermally annealed Eu^{3+}:C-$CaIn_2O_4$ of small core–shell crystallites at 400 °C for 2 h in air; (a) 0.1, (b) 0.5, (c) 1.0, and (d) 2.0 mol% Eu^{3+}-dosages, with associated energy-levels in the insets

from the energy-level diagram, the ground state multiplet ^7F_J (0, 1, 2, 3, 4, 5, 6) is more sensitized in propagating the emissions from different levels of the excited state $^5D_{J'}$ multiplet (J′ = 0, 1, 2, 3, 4). Further, the results of the light-emission observed in the samples annealed at 600 °C for 2 h in air are composed in Fig. 18. As marked in the individual bands, the $^5D_{J'} \rightarrow {}^7F_J$ transitions are significantly modified over those in the above samples in a duly modified core–shell structure.

In Fig. 19a, we compared the light-emission in a critically $Q_c \sim 0.5$ mol% Eu^{3+} doped C-$CaIn_2O_4$ before and after optimally annealed at 400 °C and 600 °C for 2 h in air, showing a way in a refined core–shell structure promotes a maximum light-emission in this hybrid structure. Qualitatively, the first band group perceives an order of enhanced intensity over 300–580 nm regime, while the second band group obtains two order of enhanced intensity over 580–900 nm regime, in the annealed samples. Obviously, only a molecularly thin grafted C-sp^2 surface is required in harvesting an enhanced light-emission of a broad band over UV–visible regions in a hybrid Eu^{3+}:C-$CaIn_2O_4$ core–shell structure. As shown in Fig. 19b, also the excitation spectrum reveals a maximum intensity in optimally annealed samples only, showing a maximum value in a $Q_c \sim 0.5\%$ Eu^{3+} doped C-$CaIn_2O_4$ sample as on it is annealed at 600 °C for 2 h in air. As a result, it is confessing an inherent correlation between the emission and the extraction spectra in this example. Here, characteristically sharp Eu^{3+} bands are merged in markedly broad bands of the multiple $^5D_{J'} \rightarrow {}^7F_J$ transitions mediated through a presumably grafted C-sp^2 surface layer of a conjoint network. As a result, also a Eu^{3+}-decorated graphene is

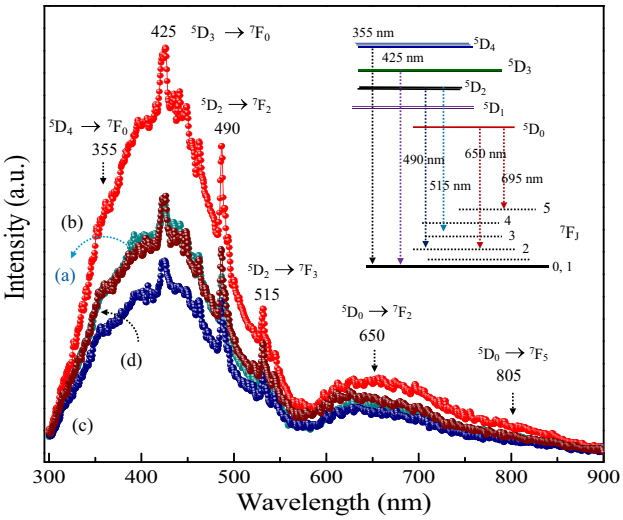

Fig. 19 (a) Light-emission ($\lambda_{ex} = 240$ nm) in a critical $Q_c \sim 0.5$ mol% Eu^{3+} doped C-$CaIn_2O_4$ before and after annealed at 400 °C and 600 °C for 2 h in air, with (b) excitation spectra ($\lambda_{em} = 512$ nm) of different Eu^{3+}:C-$CaIn_2O_4$ samples as described in the insets

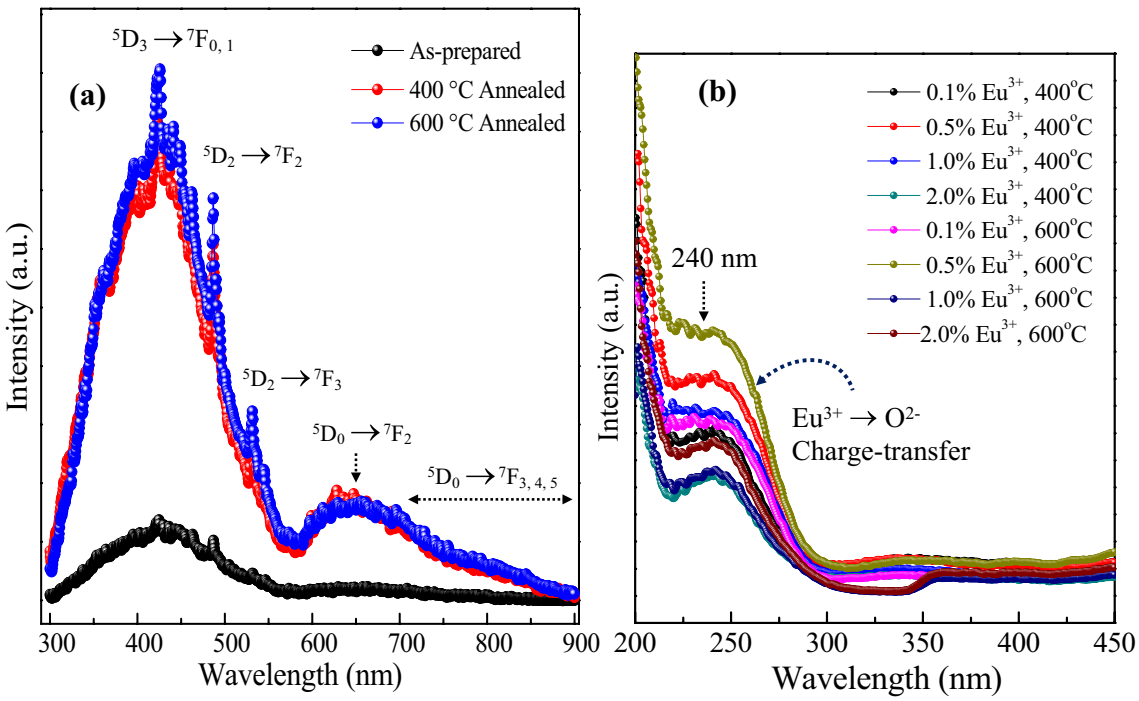

Fig. 18 **a** Light-emission ($\lambda_{ex} = 240$ nm) in thermally annealed Eu^{3+}:C-$CaIn_2O_4$ of small core–shell crystallites in as-prepared, 400 and 600 °C for 2 h in air for 1 mol% Eu^{3+}-dosages, **b** Light absorption for 0.1, 0.5, 1, 2 mol% Eu^{3+}-dosages for 400 and 600 °C annealed Eu^{3+}:C-$CaIn_2O_4$

reported of promptly combining the otherwise sharp $^5D_J' \rightarrow {}^7F_J$ (Eu^{3+}) bands in the form of a single broad blue-emission only [38]. As marked over the spectra, a metal to ligand "$Eu^{3+} \rightarrow O^{2-}$" charge-transfer [37] in a stable interface results in a prominent 240 nm excitation band irrespective of irradiating the samples at any λ_{em}-values of the emission bands. In fact, it is a core–shell Eu^{3+}:C-$CaIn_2O_4$ structure that promptly channels a strong spontaneous "$Eu^{3+} \rightarrow O^{2-}$" charge-transfer (also energy-transfer), resulting in a concomitantly surface enhanced light-emission in the UV–visible regions as long as irradiating the sample within its wide 200–300 nm regime.

Figure 20 displays a CIE chromaticity diagram estimated using the light-emission spectra observed over 300–580 nm region for a typical Eu^{3+}:C-$CaIn_2O_4$ sample having a critical $Q_c \sim 0.5$ mol% Eu^{3+} doping, so as it exhibits a maximum emission intensity in the as-prepared sample as well as when it is optimally annealed at 400 °C and 600 °C for 2 h in air. The CIE co-ordinates so obtained for these three samples are given in Table 3 in the right in Fig. 20. In these three Eu^{3+}:C-$CaIn_2O_4$ samples, the co-ordinates are varied very marginally as x = 0.15, y = 0.13 for the as-prepared sample, x = 0.18, y = 0.17 for the 400 °C annealed sample, while x = 0.22, y = 0.20 for the 600 °C annealed sample, which are all in a primarily blue light emission zone. A similar bulk sample Eu^{3+}:$CaIn_2O_4$ is well-known to serve to be a white light-emitter [38]. Another similar oxide phosphor Eu^{3+}:Y_2O_3 (0.5–1.5 mol% Eu^{3+} ions) is known to display a primarily red emission [32]. A comparison of all these results implies that an average visible color can be very finely tuned in such oxides depending on their local microscopic structure.

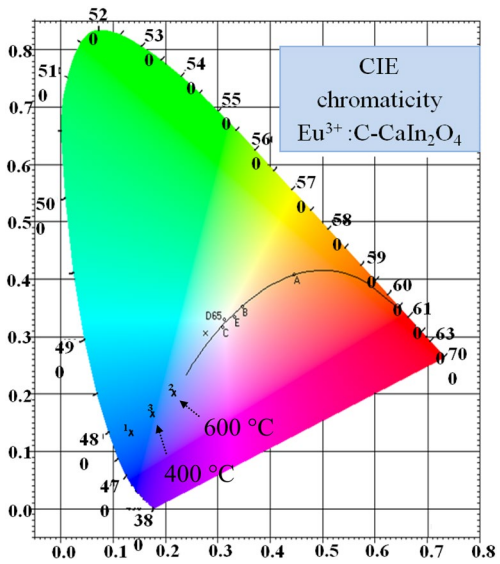

Fig. 20 CIE chromaticity of as-prepared and annealed 0.5 mol% Eu^{3+}:C-$CaIn_2O_4$ at 400 °C and 600 °C for 2 h in air, with the (x, y) co-ordinates given in the right

Table 3 CIE coordinates in Eu^{3+}:C-$CaIn_2O_4$ core–shell crystallites

Eu^{3+}:C-$CaIn_2O_4$	X	Y
As-prepared	0.15	0.13
Annealed, 400 °C, 2 h	0.18	0.17
Annealed, 600 °C, 2 h	0.22	0.20

5 Conclusions

An in situ chemical $Eu^{3+} \rightarrow In^{3+}$ doping (0–2.0 mol% Eu^{3+} dosages) of a compound $CaIn_2O_4$ by using a biogenic synthesis in this work finely tailors its lattice parameters of a high-energy t-$CaIn_2O_4$ polymorph of small Eu^{3+}:C-$CaIn_2O_4$ crystallites. It promotes a phase o → t-$CaIn_2O_4$ transformation in the annealed samples at moderate temperature 400–600 °C in air. As analyzed in terms of the XRD patterns and HRTEM studies, part of Eu^{3+} ions used here occupies the In^{3+} sites in a spinel structure and the other orders on the resulting crystallites in a hierarchical core–shell structure. An inbuilt surface C-sp^2 layer shares multiple D and G phonon bands of 1200–1800 cm^{-1} in Raman spectra of the as-prepared and optimally annealed samples (synthesized of selective compositions) of finely tuned facets on a duly modified surface C-sp^2 structure. A core–shell distinctly exhibits Eu3*d*, O1*s* and C1s XPS bands in two microscopic parts of core and shell in a hybrid structure. An optical doping of Eu^{3+} ions in selective dosages (up to 1 mol%) in a parent C-$CaIn_2O_4$ lattice of an insulator, as prepared of tunable core–shell crystallites, promptly adds and tailors multiple electronic bands in UV–visible region of the solar energy. As on thinning down part of a thin inbuilt C-sp^2 surface layer (shell) binding over a doped $CaIn_2O_4$ lattice by thermal anneals at 400–600 °C in air, it finely tunes the characteristic light absorption and emission bands in three microscopic regimes of core, interface and the surface layer in a hierarchical core–shell structure. In general, the Eu^{3+} ions exhibit a broad light emission in two major groups (1) 300–600 nm and (2) 600–900 nm of multiple bands in the optimally annealed samples. As a result, a co-doping of Eu^{3+} ions thus can conduct an efficient energy-transfer between pertinent energy levels useful for energy conversion, photocatalysis and other applications.

Acknowledgements The authors gratefully thank the Ministry of the Human Resource and Development, Government of India, for part of the financial support.

Compliance with ethical standards

Conflict of interest The authors declare that they have no conflict of interest.

References

1. Ram S, Mishra A, Fecht H-J (2010) Photoluminescence in Eu^{3+}:Al_2O_3 hybrid nanocomposites. In: Nalwa HS (ed) Encyclopedia of nanoscience and nanotechnology. American Scientific Publishers, New York
2. Haley T (1979) Toxicity. In: Gschneidner K, Eyring L (eds) Handbook on the physics and chemistry of rare earths, vol 4. North Holland, Amsterdam, p 553
3. Lafuerza S, García J, Subías G, Blasco J, Martín JH, Pascarelli S (2003) Electronic states of RFe_2O_4 (R = Lu, Yb, Tm, Y) mixed-valence compounds determined by soft cloister. Fundamentals of materials science and engineering. Wiley, New York
4. Jeon S, Braun PV (2003) Hydrothermal synthesis of Er-doped luminescent TiO_2 nanoparticles. Chem Mater 15:1256. https://doi.org/10.1021/cm0207402
5. Sole JG, Bausa LE, Jaque D (2005) An introduction to the optical spectroscopy of inorganic solids. Wiley, New York
6. Yin J, Xiang L, Zhao X (2007) Monodisperse spherical mesoporous Eu-doped TiO_2 phosphor particles and the luminescence properties. Appl Phys Lett 90:112. https://doi.org/10.1063/1.2712495
7. Li L, Tsung C-K, Yang Z, Stucky GD, Sun L, Wang J, Yan C (2008) Rare-earth-doped nanocrystalline titania microspheres emitting luminescence via energy transfer. Adv Mater 20:903. https://doi.org/10.1002/adma.200701507
8. Sandoval S, Yang J, Alfaro JG, Liberman A, Makale M, Chiang CE, Schuller IK, Kummel AC, Trogler WC (2012) Europium-doped TiO_2 hollow nanoshells: two-photon imaging of cell binding. Chem Mater 24:4222. https://doi.org/10.1021/cm302642g
9. Li T, Guo C, Jiao H, Li L, Agrawal DK (2014) Infrared-to-visible up-conversion luminescence of $CaIn_2O_4$ co-doped with R^{3+}/Yb^{3+} (R = Tm, Pr, Nd). Opt Commun 312:284. https://doi.org/10.1039/C5TC04302F
10. Kumar JBP, Ramgopal G, Vidya YS, Anantharaju KS, Prasad BD, Sharma SC, Prashantha SC, Nagaswarupa HP, Kavyashree D, Nagabhushana H (2015) Green synthesis of Y_2O_3:Dy^{3+} nanophosphor with enhanced photocatalytic activity. Spectrochim Acta A 149:687. https://doi.org/10.1016/j.saa.2015.05.007
11. Liu X, Li C, Quan Z, Cheng Z, Lin J (2007) Tunable luminescence properties of $CaIn_2O_4$:Eu^{3+} phosphors. J Phys Chem C 111:16601. https://doi.org/10.1021/jp074868o
12. Yan W, Zhang Y, Xie W, Sun S, Ding J, Bao J, Gao C (2014) $CaIn_2O_4$/Fe–TiO_2 composite photocatalysts with enhanced visible light performance for hydrogen production. J Phys Chem C 118:6077. https://doi.org/10.1021/jp412810n
13. Chandran SP, Chaudhary M, Pasricha R, Ahmad A, Sastry M (2006) Synthesis of gold nanotriangles and silver nanoparticles using *aloe vera* plant extract. Biotechnol Progr 22:577. https://doi.org/10.1021/bp0501423
14. Manikandan A, Sridhar R, Antony SA, Ramakrishna S (2014) A simple aloe vera plant-extracted microwave and conventional combustion synthesis: morphological, optical, magnetic and catalytic properties of $CoFe_2O_4$ nanostructures. J Mol Struct 1076:188. https://doi.org/10.1016/j.molstruc.2014.07.054
15. Mohanty P, Ram S (2003) Enhanced photoemission in dispersed Eu_2O_3 nanoparticles in amorphous Al_2O_3. J Mater Chem 13:3021. https://doi.org/10.1039/B307028J
16. Mondal A, Ram S (2008) Enhanced phase stability and photoluminescence of Eu^{3+} modified t-ZrO_2 nanoparticles. J Am Ceram Soc 91:329. https://doi.org/10.1111/j.1551-2916.2007.02137.x
17. Mishra A (2009) Microstructure and optical properties in nanofluids and films of gold nanoparticles in poly(vinyl pyrrolidone). PhD thesis, Indian Institute of Technology, Kharagpur, India
18. X-ray powder diffraction JCPDS files, (a) 01-071-3853, t-CaIn2O4), (b) 04-009-1239, o-CaIn2O4), and (c) 04-007-2081 (graphite), Joint Committee on Powder Diffraction Standard International Centre for Diffraction Data, Swarthmore, PA, USA, 2013
19. Tiwari B, Ram S, Banerji P (2018) Biogenic synthesis of tunable core–shell C-CaIn2O4, interface bonding, conductive network channels, and tailored dielectric properties. ACS Sustain Chem Eng 6:16298. https://doi.org/10.1021/acssuschemeng.8b03197
20. Williamson GK, Hall WH (1953) X-ray line broadening from filed aluminium and wolfram. Acta Metall 1:22. https://doi.org/10.1016/0001-6160(53)90006-6
21. Ram S (2001) Self-confined dimension of thermodynamic stability in co-nanoparticles in fcc and bcc allotropes with a thin amorphous Al_2O_3 surface layer. Acta Mater 49:2297. https://doi.org/10.1016/S1359-6454(01)00113-6
22. Mohanty P, Ram S (2002) Confined growth in Eu_2O_3 nanocrystals in a new polymorph in an amorphous mesoporous Al_2O_3. Philos Mag B 82:1129. https://doi.org/10.1080/13642810208223154
23. Wang YY, Ni ZH, Yu T, Shen ZX, Wang HM, Wu YH, Chen W, Wee ATS (2008) Raman studies of monolayer graphene: the substrate effect. J Phys Chem C 112:10637. https://doi.org/10.1021/jp8008404
24. Misra S, Karan T, Ram S (2015) Dynamics of surface spins in small core–shell magnets of $Li_{0.35}Zn_{0.35}Fe_{2.35}O_4$ bonds over a carbon surface and tailored magnetic properties. J Phys Chem C 119:23184. https://doi.org/10.1021/acs.jpcc.5b04635
25. Ross SD (1972) Inorganic infrared and Raman spectra. McGraw-Hill, England
26. Tang J, Zou Z, Ye J (2004) Effects of substituting Sr^{2+} and Ba^{2+} for Ca^{2+} on the structural properties and photocatalytic behaviors of $CaIn_2O_4$. Chem Mater 16:1644. https://doi.org/10.1021/cm0353815
27. Zheng HL, Zhang ZC, Zhou JG, Yang SS, Zhao J (2012) Vibrational spectra of $CaGa_2O_4$, Ca_2GeO_4, $CaIn_2O_4$ and $CaSnO_3$ prepared by electro-spinning. Appl Phys A 108:465. https://doi.org/10.1007/s00339-012-6916-4
28. Shen J, Hu Y, Shi M, Li N, Ma H, Ye M (2010) One step synthesis of graphene oxide–magnetic nanoparticle composite. J Phys Chem C 114:1498. https://doi.org/10.1021/jp909756r
29. Du Y, Liu W, Qiang R, Wang Y, Han X, Ma J, Xu P (2014) Shell thickness-dependent microwave absorption of core-shell Fe_3O_4@C composites. ACS Appl Mater Interfaces 6:12997. https://doi.org/10.1021/am502910d
30. Ge L (2007) Preparation of novel visible-light-driven In_2O_3–$CaIn_2O_4$ composite photocatalyst by sol–gel method. J Sol-Gel Sci Technol 44:263. https://doi.org/10.1007/s10971-007-1620-0
31. Wagner CD, Riggs WM, Davis LE, Moulder JF, Mullenberg GE (1979) Handbook of X-ray photoelectron spectroscopy. Perkin-Elmer Corporation, Eden Prairie, Minnesota
32. Zhang Y, Selvaraj R, Sillanpaa M, Kim Y, Tai CW (2014) Co-precipitates synthesis of $CaIn_2O_4$ and its photocatalytic degradation of methylene blue by visible light irradiation. Ind Eng Chem Res 53:11720. https://doi.org/10.1021/ie403401y
33. Sharma SK, Rajeswari PV, Tiwari B, Ram S (2017) Hydrothermal synthesis of $LiMnPO_4$-C(sp^2) hybrids, conductive channels, and enhanced dielectric permittivity: a modulated ionic conductor. Ionics 23:43. https://doi.org/10.1007/s11581-016-1800-4
34. Rajeswari PV, Tiwari B, Ram S, Pradhan D (2018) A biogenic TiO_2–C–O nanohybrid grown from a Ti^{4+}-polymer complex in

green tissues of chilis, interface-bonding and tailored photocatalytic properties. J Mater Sci 53:3131. https://doi.org/10.1007/s10853-017-1763-5
35. Tiwari B, Ram S, Banerji P (2017) Aloe-vera mediated synthesis of Eu^{3+} doped $CaIn_2O_4$-carbon hybrid nanostructure and its light emission properties. MRS Adv 2:141. https://doi.org/10.1557/adv.2016.674
36. Mohanty P, Ram S (2006) Light emission associated with the $^5D_0 \rightarrow {}^7F_3$ forbidden transition in Eu^{3+} cations dispersed in a Eu^{3+}:Al_2O_3 mesoporous structure. Philos Mag Lett 86:375. https://doi.org/10.1080/09500830600820985
37. Ram S, Fecht H-J (2011) Modulating up-energy transfer and violet-blue light emission in gold nanoparticles with surface adsorption of poly(vinyl pyrrolidone) molecules. J Phys Chem C 115:7817. https://doi.org/10.1021/jp105941h
38. Park B, Kim SJ, Lim J, Some S, Park J-E, Kim S-J, Kim C, Leed TJ, Jun SC (2015) Tunable wide blue photoluminescence with europium decorated graphene. J Mater Chem C 3:4030. https://doi.org/10.1039/C4TC02361G